



An explicit stabilised finite element method for Navier-Stokes-Brinkman equations

Loic Balazi Atchy Nillama^{a,b}, Jianhui Yang^{b,*}, Liang Yang^{a,*}

^a Division of Energy and Power, Cranfield University, UK

^b Geoscience Research Centre, TOTAL E&P UK Limited, UK

ARTICLE INFO

Article history:

Received 26 August 2021

Received in revised form 27 January 2022

Accepted 28 January 2022

Available online 10 February 2022

Keywords:

Stabilised finite element method

Unified Navier-Stokes-Brinkman formulation

Grayscale micro-CT image

Micro-porosity

ABSTRACT

We present an explicit stabilised finite element method for solving Navier-Stokes-Brinkman equations. The proposed algorithm has several advantages. First, the lower equal-order finite element space for velocity and pressure is ideal for presenting the pixel images. Stabilised finite element allows the continuity of both tangential and normal velocities at the interface between regions of different micro-permeability or at the interface free/porous domain. Second, the algorithm is fully explicit and versatile for describing complex boundary conditions. Third, the fully explicit matrix-free finite element implementation is ideal for parallelism on high-performance computers. In the last, the implicit treatment of Darcy term allowed larger time stepping and a stable computation, even if the velocity varies for several orders of magnitude in the micro-porous regions (Darcy regime).

The stabilisation parameter, that may affect the velocity field, has been discussed and an optimal parameter was chosen based on the numerical examples. Velocity stability at interface between different micro-permeability has been also studied with mesh refinement. We analysed the influence of the micro-permeability field on the regime of the flow (Stokes flow, Darcy flow or a transitional regime). These benchmark tests provide guidelines for choosing the resolution of the grayscale image and its segmentation. We applied the method on real Berea Sandstone micro-CT images, and proceeded the three-phases segmentation. We studied the influence of the micro-porosity field, using the well-known Kozeny-Carman relation to derive the micro-permeability field from the micro-porosity field, on the effective permeability computed. Our analysis shows that a small fraction of micro-porosity in the rock has a significant influence on the effective permeability computed.

© 2022 Elsevier Inc. All rights reserved.

1. Introduction

Understanding the flow over porous media and calculation of permeability is important in petroleum engineering, earth science and engineering and environmental problems. Permeability is an intrinsic property of the complex micro-structure, and difficult to find the empirical correlation of the permeability with porosity or other properties [1]. Soulaire et al. [2] studied the impact of sub-resolution porosity of X-ray micro-CT images on the permeability. By considering the micro-

* Corresponding authors.

E-mail addresses: jianhui.yang@total.com (J. Yang), Liang.Yang@cranfield.ac.uk (L. Yang).

porosity at the pore scale, the Navier-Stokes equations are insufficient to solve the flow. The Darcy equation which governs the flow in porous media should be considered. It leads to the so-called Navier-Stokes-Brinkman equations.

With the development of micro-CT imaging techniques, we can now have access to the pore space with an increasingly fine resolution of different kinds of rocks such as sandstone or carbonate. It is possible to perform numerical simulations of the flow directly on the grayscale micro-CT images. This new approach, named digital rock physics, is recognised as a replacement to conventional laboratory approaches, and provides a better understanding of the rock properties. In the last few years, many techniques have been exploited to compute the flow directly on micro-CT images. One numerical method is the lattice Boltzmann method (LBM), which solves a discrete mesoscale form of Boltzmann equation directly on a voxel grid of segmented images. It is widely adopted in simulating flow and reactive transport in porous media due to its easy implementation and treatment of boundaries in complex geometries. It is also suited for parallel computing with a high computational efficiency. This approach has been adopted to investigate the porous flow directly on micro-CT images [3–9]. The other popular approach is the Finite Volume method (FVM). It allows to use an adaptive grid to reduce the number of grid cells rather than a regular grid on a 3D pore space image. FVM is fast for high-porosity structures, but requires more iterations for low-porosity structures to reach desired accuracy [6]. The convergence speed relies on the complexity and heterogeneity of the porous medium, and it is challenging to simulate slip boundary conditions [2,10–14]. Recently, Yang et al. [15] used the stabilised Finite Element method (FEM) for the simulations of absolute permeability by solving the Navier-Stokes equations directly on binarised micro-CT images. The method was the first efficient FEM based calculation for 3D micro-CT images. In this work, we proposed to extend the method [15] to solve Navier-Stokes-Brinkman equations on grayscale micro-CT images. Similar approaches have been developed for solving the coupled Darcy-Stokes flow on the reservoir scale [16–18].

Solving the flow on grayscale micro-CT images raises many numerical challenges. With the increased resolution, micro-CT images can contain millions or billions of voxels leading to a high computational cost. In addition, porous media are highly heterogeneous with discontinuity on physical properties, e.g. permeability and porosity. Dealing with different length scales and large (ten orders of magnitude) contrasts in permeability leads to ill-conditioned linear systems of equations and direct computation is often impracticable [16]. The flow is governed by Stokes equations in free regions and by Darcy equations in porous regions. The main numerical challenge is thus to consider interfaces between regions of different permeability. The pressure gradient changes drastically at the interface due to the variation of κ_{micro} and needs to be carefully evaluated for accurate and stable computation. The transition zone at the interface, where the flow changes drastically, is estimated to be of the order of $\sqrt{\kappa_{\text{micro}}}$ [19]. A fine resolution is required to resolve the transition zone.

In general, there are mainly two approaches to solve flow equations in porous media: two domain approach and single domain approach (unified formulation). In the two domain approaches, two different sets of governing equations are used to describe the flows in the fluid and the porous domains. Classically Navier-Stokes equations are solved in the free regions whereas Darcy equations are solved in the porous regions [16,19]. The set of equations are completed by interface condition to enforce the continuity. Various interface conditions have been developed and intensively discussed [20]. This method is adapted for domains where the interface between free and porous region is clearly defined with different layers. However, for grayscale images, this method does not appear suitable given the large number of interfaces and involves the definition of an interface matrix linked to porosity and permeability matrix. The second approach is the single domain method with an unified formulation for Stokes-Brinkman equations. It avoids imposing the interface conditions. It is the most suitable to solve the flow on grayscale micro-CT images given the complexity and a number of interfaces. Although the implementation of this proposed method is more straightforward, it may result in inaccurate flow field near the interface [19].

Many researchers have work on unified formulation of Stokes-Darcy equations using FEM [21–23]. One numerical challenge to solve the unified Navier-Stokes-Brinkman equations is that the Galerkin approximation of both the Stokes and the Darcy problems requires the use of velocity-pressure interpolations that satisfy the adequate inf-sup conditions [24]. Different interpolation pairs are known to satisfy this condition for each problem independently, but the key issue is to find interpolations that satisfy both at the same time. In case of Darcy flow, numerical error is introduced when using a discretisation with a continuous velocity field leading to an error which depends on the mesh resolution [16].

Different approaches were proposed to overcome this difficulty. Using Galerkin technique and mixed FE formulations can satisfy the inf-sup conditions, e.g. the combination of the Raviart–Thomas FE velocity space with piece-wise constant or linear pressures [16,24]. Discretising Darcy equations using elements with a continuous normal velocity component and a discontinuous tangential velocity component such as Raviart–Thomas elements allows to obtain a correct solution. However, these elements are not suitable for the Stokes case and are restricted to specific typologies of meshes. In particular this method cannot be directly applied on binarised three-dimensional images. The second alternative is to invoke the Darcy law in the mass conservation equation leading to a pressure Poisson problem, an elliptic problem that can be easily approximated by the Galerkin technique and Lagrangian elements. However as noted by [24], this technique leads to the loss of accuracy for the velocity and the very weak enforcement of the mass conservation equation. The third alternative is the use of stabilised FEM which allow the use of any velocity-pressure pair. Different stabilised finite element methods have been proposed in the literature such as Galerkin/Least-Squares (GLS) [25–27], Streamline-Upwind/Petrov–Galerkin (SUPG) [28–30], Pressure-Stabilising/Petrov–Galerkin (PSPG) [31–33], Pressure Gradient Projection (SPGP) [34,35,25] or Variational Multi-Scale method (VMS) [36,37,24,21,38,39], among others [40]. However as noted in [41–43], the choice of an optimal stabilisation parameter is difficult, which is often based on heuristic methods and analysis of numerical results. The parameter affects the accuracy of the numerical approximation.

In this work we propose to implement a stabilised FEM by using the Variational Multiscale (VMS) approach which consists in splitting the unknowns in large scale and sub-grid scale components and which has demonstrated that the same formulation works for the Stokes and the Darcy problems [21–23]. It allows the use of linear equal-order velocity and pressure interpolation defined on the same nodes which is ideal for describing the boundary condition in the simulation of flow through rock images. Applying the non-slip boundary conditions and constant pressure boundary conditions is simple and straightforward. Moreover, the use of trilinear discretisation coupled with stabilised FEM allows the continuity of both tangential and normal velocity at interface between regions of different micro-permeability. The explicit stabilised FEM allows us to solve the Navier-Stokes equations with reduced memory costs on large computational domain. In the proposed formulation, the use of the artificial compressibility with the introduction of a time derivative of the pressure in the mass continuity equation allows to treat the Darcy part implicitly and keep the whole algorithm explicit. The implicit Darcy term allows the use of larger time stepping making it possible grayscale simulation on digital rock containing more than 800^3 voxels.

2. Governing equations

2.1. Navier-Stokes-Brinkman equations

The average Navier-Stokes-Brinkman equations are defined as [2]:

$$-\frac{\nu}{\epsilon_{\text{micro}}} \nabla^2 \bar{\mathbf{u}} + \bar{\mathbf{u}} \cdot \nabla \bar{\mathbf{u}} + \nabla \bar{p} + \nu \kappa_{\text{micro}}^{-1} \bar{\mathbf{u}} = \mathbf{f} \quad (1)$$

$$\nabla \cdot \bar{\mathbf{u}} = 0$$

where ϵ_{micro} and κ_{micro} are the micro-porosity and the micro-permeability field respectively, \bar{p} is the phase average pressure and $\bar{\mathbf{u}}$ is the volume-average velocity (superficial average) equivalent to the Darcy velocity defined as:

$$\bar{\mathbf{u}} = \frac{1}{V_f} \int_{V_f} \mathbf{u} dV \quad (2)$$

$$\bar{p} = \frac{1}{V_f} \int_{V_f} p dV$$

where V_f is the volume occupied by the fluid in the control volume V .

Generally the relations between micro-porosity ϵ_{micro} and micro-permeability κ_{micro} are in the form

$$\begin{aligned} g: [0; 1] &\longrightarrow [0; +\infty[\\ \epsilon_{\text{micro}} &\longmapsto f(\epsilon_{\text{micro}}) = \kappa_{\text{micro}} \end{aligned} \quad (3)$$

with

$$\begin{aligned} g(0) &= 0 \\ g(1) &= +\infty \\ g' &> 0 \end{aligned}$$

This general equation allows to switch asymptotically from the continuum behaviour, where Darcy flow is dominant ($\kappa_{\text{micro}} \rightarrow 0$) to the Navier-Stokes flow ($\kappa_{\text{micro}} \rightarrow \infty$) according to the cell porosity values, such as,

- when the micro-permeability $\epsilon_{\text{micro}} = 1$, we have Stokes flow and $\bar{\mathbf{u}} = \mathbf{u}$
- when the micro-permeability $0 < \epsilon_{\text{micro}} < 1$, we have Darcy flow and $\bar{\mathbf{u}} = -\frac{\kappa_{\text{micro}}}{\nu} \nabla \bar{p}$ (Darcy's Law)

From now, \mathbf{u} and p will be denoted for phase average velocity and phase averaged pressure for simplicity.

2.2. Pseudo-compressible form

The artificial compressibility formulation [44] replaces the divergence free constraint by adding a pseudo-time derivative of the pressure. Navier-Stokes-Brinkman system (4) is modified to

$$\begin{aligned} \partial_t \mathbf{u} - \nu \nabla^2 \mathbf{u} + \epsilon_{\text{micro}} \mathbf{u} \cdot \nabla \mathbf{u} + \epsilon_{\text{micro}} \nabla p + \nu \epsilon_{\text{micro}} \kappa_{\text{micro}}^{-1} \mathbf{u} &= \epsilon_{\text{micro}} \mathbf{f} \\ \partial_t p + \zeta^{-1} \nabla \cdot \mathbf{u} &= 0 \end{aligned} \quad (4)$$

If we denoted $\sigma = \nu \epsilon_{\text{micro}} \kappa_{\text{micro}}^{-1}$, then

$$\begin{aligned} \partial_t \mathbf{u} - \nu \nabla^2 \mathbf{u} + \epsilon_{\text{micro}} \mathbf{u} \cdot \nabla \mathbf{u} + \epsilon_{\text{micro}} \nabla p + \sigma \mathbf{u} &= \epsilon_{\text{micro}} \mathbf{f} \\ \partial_t p + \zeta^{-1} \nabla \cdot \mathbf{u} &= 0 \end{aligned} \quad (5)$$

In Equation (5), ζ^{-1} is the artificial compressibility coefficient, where a pseudo sound speed can be written as $c = \sqrt{\zeta^{-1}}$. When the wave speed $c \rightarrow \infty$, Equation (5) approximates Equation (1). A relaxation of the divergence free will allow to use fully explicit temporal discretisation methods. For the rock image calculation, a steady state solution is required and the coefficient will not affect the final solution as $\partial_t p \rightarrow 0$. With the artificial compressibility, the equations become a hyperbolic system, and a Courant number less than one is required for temporal stability for explicit methods. The Courant number restriction is written as:

$$\Delta t \leq \beta \frac{\Delta x}{c} \quad (6)$$

where β is a safe coefficient and Δx is the minimum cell size. The porous media flow is a diffusion-dominated problem (Reynolds Number $Re \ll 1$), a diffusive velocity (that should be smaller than the sound wave speed c) can be defined as,

$$v_{\text{diff}} = \frac{2}{hRe} \quad (7)$$

with h is the cell size.

2.3. Weak formulation and notation

It is necessary to introduce some notations to obtain the weak form. Let's denote by $L^2(\Omega)$ the spaces of functions that are square integrable in Ω with respect to the Lebesgue measure. It is a Hilbert space with scalar product $(\mathbf{u}, \mathbf{v})_\Omega \equiv (\mathbf{u}, \mathbf{v}) = \int_\Omega \mathbf{u}(x) \mathbf{v}(x) d\Omega$. The integral is performed over a subdomain ω by $(\cdot, \cdot)_\omega$. $H^1(\Omega)$ denotes the Sobolev space of square integrable functions with square integral derivative as:

$$H^1(\Omega) = \{\mathbf{u} : \Omega \rightarrow \mathbb{R} \mid \mathbf{u}, \nabla \mathbf{u} \in L^2(\Omega)\} \quad (8)$$

The solution $H_E^1(\Omega)$ space and the test space H_0^1 are defined by:

$$\begin{aligned} H_E^1(\Omega) &= \{\mathbf{u} \in H^1(\Omega)^d \mid \mathbf{u} = \bar{\mathbf{u}} \text{ on } \Gamma\}, \\ H_0^1(\Omega) &= \{\mathbf{u} \in H^1(\Omega)^d \mid \mathbf{u} = \mathbf{0} \text{ on } \Gamma\}. \end{aligned} \quad (9)$$

Furthermore, $H^{-1}(\Omega)$ denotes the topological dual of $H_0^1(\Omega)$ and $\langle \cdot, \cdot \rangle$ the duality pairing between $H^{-1}(\Omega)$ and $H_0^1(\Omega)$. Then, the standard weak form of Equation (5) is the following: for each time t , find a velocity $\mathbf{u}(t) \in H_E^1(\Omega)$ and a pressure $p(t) \in L^2(\Omega)$ such that

$$\begin{aligned} (\partial_t \mathbf{u}, \mathbf{v}) + \nu (\nabla \mathbf{u}, \nabla \mathbf{v}) - (p, \nabla \cdot \mathbf{v}) + (\mathbf{u} \cdot \nabla \mathbf{u}, \mathbf{v}) + \sigma (\mathbf{u}, \mathbf{v}) &= (\mathbf{f}, \mathbf{v}) \text{ for all } \mathbf{v} \in H_0^1(\Omega) \\ (\partial_t p, q) + \zeta^{-1} (\nabla \cdot \mathbf{u}, q) &= 0 \text{ for all } q \in L^2(\Omega) \end{aligned} \quad (10)$$

3. Stabilised finite element

3.1. Variational multiscale formulation

We will use the VMS method developed in [44]. This method decomposes the solution \mathbf{u} and p on a large scale component and a sub-scale component. The large scale components \mathbf{u}_h and p_h are resolved in the FE mesh, whilst the sub-scale components $\tilde{\mathbf{u}}$ and \tilde{p} are approximated by a certain analytical approach. We decompose spaces $H_E^1(\Omega)$ and $L^2(\Omega)$ such that $H_E^1(\Omega) = \mathbf{V}_h \oplus \tilde{\mathbf{V}}$ and $L^2(\Omega) = L_h \oplus \tilde{L}$, where $\tilde{\mathbf{V}}$ and \tilde{L} denote the infinite-dimensional spaces that complete the FE spaces \mathbf{V}_h and L_h to approximate the velocity and pressure in the standard Galerkin FE method. $(\cdot)_h$ and $(\tilde{\cdot})$ denote the FE component and the sub-grid component, respectively. Thus, we approximate the velocity \mathbf{u} and pressure p by

$$\mathbf{u} \approx \mathbf{u}_h + \tilde{\mathbf{u}} \quad p \approx p_h + \tilde{p}$$

where $\mathbf{u}_h \in \mathbf{V}_h$, $\tilde{\mathbf{u}} \in \tilde{\mathbf{V}}$, $p_h \in L_h$ and $\tilde{p} \in \tilde{L}$ for each time t . Using this splitting in 10 yields

$$\begin{aligned} (\partial_t (\mathbf{u}_h + \tilde{\mathbf{u}}), \mathbf{v}) + \nu (\nabla (\mathbf{u}_h + \tilde{\mathbf{u}}), \nabla \mathbf{v}) - (p_h + \tilde{p}, \nabla \cdot \mathbf{v}) \\ + ((\mathbf{u}_h + \tilde{\mathbf{u}}) \cdot \nabla (\mathbf{u}_h + \tilde{\mathbf{u}}), \mathbf{v}) + \sigma (\mathbf{u}_h + \tilde{\mathbf{u}}, \mathbf{v}) &= (\mathbf{f}, \mathbf{v}) \\ (\partial_t (p_h + \tilde{p}), q) + \zeta^{-1} (\nabla \cdot (\mathbf{u}_h + \tilde{\mathbf{u}}), q) &= 0 \end{aligned} \quad (11)$$

3.2. FE scale problem

Codina [37] proposed to enforce the sub-scales to be orthogonal to the FE velocity and pressure spaces. We choose to use this approach in this paper. Thus, we choose the sub-grid spaces to be orthogonal in the $L^2(\Omega)$ to the FE spaces. Therefore the time derivative terms $(\partial_t \tilde{\mathbf{u}}, \mathbf{v}_h)$ and $(\partial_t \tilde{p}, q_h)$ as well as the term $\sigma(\tilde{\mathbf{u}}, \mathbf{v}_h)$ vanish:

$$\begin{aligned} (\partial_t(\mathbf{u}_h + \tilde{\mathbf{u}}), \mathbf{v}_h) &= (\partial_t \mathbf{u}_h, \mathbf{v}_h); \quad (\partial_t(p_h + \tilde{p}), q_h) = (\partial_t p_h, q_h) \\ \sigma(\mathbf{u}_h + \tilde{\mathbf{u}}, \mathbf{v}_h) &= \sigma(\mathbf{u}_h, \mathbf{v}_h) \end{aligned}$$

the other considerations to satisfy this orthogonality in practice [44],

- The viscous term $\nu(\nabla(\mathbf{u}_h + \tilde{\mathbf{u}}), \nabla \mathbf{v}_h)$ is simplified as (by integrating by parts):

$$\begin{aligned} \nu(\nabla(\mathbf{u}_h + \tilde{\mathbf{u}}), \nabla \mathbf{v}_h) &= \nu(\nabla \mathbf{u}_h, \nabla \mathbf{v}_h) + \sum_K [(-\tilde{\mathbf{u}}, \nabla^2 \nu h)_K + (\tilde{\mathbf{u}}, n \cdot \nabla \mathbf{v}_h)_{\partial K}] \\ &= \nu(\nabla \mathbf{u}_h, \nabla \mathbf{v}_h) \end{aligned}$$

The term $(-\tilde{\mathbf{u}}, \nabla^2 \nu h)_K$ vanishes for linear elements. The term $(\tilde{\mathbf{u}}, n \cdot \nabla \mathbf{v}_h)_{\partial K}$ is usually neglected in practice.

- In order to avoid derivatives of the sub-grid component, the convective component can be re-written as:

$$\begin{aligned} \langle (\mathbf{u}_h + \tilde{\mathbf{u}}) \cdot \nabla(\mathbf{u}_h + \tilde{\mathbf{u}}), \mathbf{v}_h \rangle \\ = \langle (\mathbf{u}_h + \tilde{\mathbf{u}}) \cdot \nabla \mathbf{u}_h, \mathbf{v}_h \rangle - \langle \tilde{\mathbf{u}}, (\mathbf{u}_h + \tilde{\mathbf{u}}) \cdot \nabla \mathbf{v}_h \rangle \end{aligned}$$

where we have used the fact that $\mathbf{u}_h + \tilde{\mathbf{u}}$ is divergence free when integrating by parts. As noted in [45], for simplification, one usually takes $\mathbf{a} \approx \mathbf{u}_h$ as advection velocity.

- Again to avoid derivatives of the sub-grid scales, the mass conservation equation is re-written as:

$$\zeta^{-1}(\nabla \cdot (\mathbf{u}_h + \tilde{\mathbf{u}}), q_h) = \zeta^{-1}(\nabla \cdot \mathbf{u}_h, q_h) - \zeta^{-1}(\tilde{\mathbf{u}}, \nabla q_h) + \zeta^{-1}(n \cdot \tilde{\mathbf{u}}, q_h)_{\partial \Omega}$$

after integration by parts. As before, the sub-grid scale boundary term is neglected.

Taking into account the previous considerations, the equations we have are:

$$\begin{aligned} (\partial_t \mathbf{u}_h, \mathbf{v}_h) + \nu(\nabla \mathbf{u}_h, \nabla \mathbf{v}_h) + \langle \mathbf{u}_h \cdot \nabla \mathbf{u}_h, \mathbf{v}_h \rangle - (p_h, \nabla \cdot \mathbf{v}_h) + \sigma(\mathbf{u}_h, \mathbf{v}_h) - \langle \mathbf{f}, \mathbf{v}_h \rangle \\ - \langle \tilde{\mathbf{u}}, \mathbf{a} \cdot \nabla \mathbf{v}_h \rangle + \langle \tilde{\mathbf{u}} \cdot \nabla \mathbf{u}_h, \mathbf{v}_h \rangle - (\tilde{p}, \nabla \cdot \mathbf{v}_h) = 0 \\ (\partial_t p_h, q_h) + \zeta^{-1}(\nabla \cdot \mathbf{u}_h, q_h) - \zeta^{-1}(\tilde{\mathbf{u}}, \nabla q_h) = 0 \end{aligned} \quad (12)$$

where $\mathbf{a} = \mathbf{u}_h + \tilde{\mathbf{u}}$. The problem will be closed once an approximation for the sub-grid scale velocity and pressure is proposed.

3.3. Local sub-grid scale problem

In this section, we discuss the subgrid scale formulation and then give the analytical approximation of the solution. As a result, the orthogonal sub-grid scale in an explicit VMS method will be given. The sub-grid scale equation reads (in strong form):

$$\begin{aligned} \partial_t \tilde{\mathbf{u}} - \nu \nabla^2 \tilde{\mathbf{u}} + (\mathbf{u}_h + \tilde{\mathbf{u}}) \cdot \nabla \tilde{\mathbf{u}} + \epsilon_{\text{micro}} \nabla \tilde{p} + \sigma \tilde{\mathbf{u}} &= \mathbf{R}_u \\ \partial_t \tilde{p} + \zeta^{-1} \nabla \cdot \tilde{\mathbf{u}} &= R_p \end{aligned} \quad (13)$$

where \mathbf{R}_u and R_p are appropriate residuals of the FE components defined as,

$$\begin{aligned} \mathbf{R}_u &= -\mathcal{P}_u(\partial_t \mathbf{u}_h - \nu \nabla^2 \mathbf{u}_h + (\mathbf{u}_h + \tilde{\mathbf{u}}) \cdot \nabla \mathbf{u}_h + \epsilon_{\text{micro}} \nabla p_h + \sigma \mathbf{u}_h - \epsilon_{\text{micro}} \mathbf{f}) \\ R_p &= -\mathcal{P}_p(\partial_t p_h + \zeta^{-1} \nabla \cdot \mathbf{u}_h) \end{aligned} \quad (14)$$

\mathcal{P}_u and \mathcal{P}_p are projection operators onto the sub-grid scale spaces of velocities and pressure. In the case in which we take the identity operator in both cases, we recover the original VMS method proposed [39].

3.3.1. Velocity sub-grid problem

Next, we consider the following algebraic approximation of this nonlinear differential system. We refer to [36] for a detailed exposition of the sub-grid problem approximation, in which the stabilisation parameters are estimated using a Fourier analysis approach. After time discretisation, using an implicit-explicit first order time integration, the approximated dynamic sub-grid model for the momentum equation reads as:

$$\frac{1}{\Delta t} \tilde{\mathbf{u}}^{n+1} + \frac{1}{\tau_u^n} \tilde{\mathbf{u}}^{n+1} = \frac{1}{\Delta t} \tilde{\mathbf{u}}^n + \mathbf{R}_u \quad (15)$$

where $\frac{1}{\tau_u^n} = \frac{1}{\tau_s} + \frac{1}{\tau_c} + \frac{1}{\tau_d}$, which leads to:

$$\tilde{\mathbf{u}}^{n+1} = \frac{\tau_{ut}^n}{\Delta t} \tilde{\mathbf{u}}^n + \tau_{ut}^n \mathbf{R}_u \quad (16)$$

where $\frac{1}{\tau_{ut}^n} = \frac{1}{\Delta t} + \frac{1}{\tau_u^n}$.

τ_s , τ_c and τ_d are called stabilisation parameters, associated respectively to Stokes flow, Convective flow and Darcy flow, defined as:

$$\begin{aligned} \tau_s &= (c_1 \nu)^{-1} h^2 \\ \tau_c &= (c_2 |\mathbf{u}_h^n + \tilde{\mathbf{u}}^n|)^{-1} h \\ \tau_d &= (c_3 \sigma)^{-1} \end{aligned} \quad (17)$$

where c_1 , c_2 and c_3 are algorithmic constants.

Remark 1. The stabilisation parameter τ must vanish when the mesh is refined (no stabilisation is necessary for a fine enough mesh). Convergence is affected by the asymptotic behaviour of τ . To take into account the mesh refinement in τ_d , e.g. the cell size h , let's introduce a characteristic length scale of the problem, that we denote by l_u , as prescribed in [21]. Whereas for the Stokes problem its introduction is unnecessary, it will play a key role in the Darcy problem. The stabilisation parameter associated to the Darcy flow τ_d can be thus re-written as,

$$\tau_d = (c_3 \sigma)^{-1} \frac{h^2}{l_u^2} \quad (18)$$

The choice of l_u was discussed in [24]. For equal velocity-pressure approximations, the best accurate choice is to take l_u as $l_u = \sqrt{L_0 h}$, where L_0 is the diameter of the domain Ω , which leads to

$$\tau_d = (c_3 \sigma)^{-1} \frac{h}{L_0} \quad (19)$$

Remark 2. Since Stokes and Darcy problem are unified in this method, a comparison between τ_s and τ_d leads to:

$$\frac{\tau_s}{\tau_d} \sim \epsilon_{\text{micro}} \frac{h L_0}{\kappa_{\text{micro}}} \quad (20)$$

In case of Darcy flow we have $\kappa_{\text{micro}} \ll h L_0$ leading to $\tau_u^n \approx \tau_d$. In case of Stokes flow, $\kappa_{\text{micro}} \gg h L_0$ leading to $\tau_u^n \approx \tau_s$. The term τ_c can be neglected for stabilisation. Please note the permeability κ_{micro} varies in space, the stabilisation parameter varies also in space.

Remark 3. We can treat the sub-grid scale term implicitly because it does not imply an increase in CPU cost. Note that the previous expressions for the sub-grid scales are required at the integration points.

3.3.2. Pressure sub-grid problem

The pressure sub-grid scale component can be treated in a similar way. This component can be found from:

$$\frac{1}{\Delta t} \tilde{p}^{n+1} + \frac{1}{\tau_p^n} \tilde{p}^{n+1} = \frac{1}{\Delta t} \tilde{p}^n + R_p \quad (21)$$

where

$$\tau_p^n = (c_4 \zeta^{-1} \tau_u^n)^{-1} h^2 = c_4 \zeta^{-1} (c_1 \nu + c_2 |\mathbf{u}_h^n + \tilde{\mathbf{u}}^n| h + c_3 \sigma l_u^2) \quad (22)$$

τ_p^n is homogeneous to a time and c_4 being an algorithmic constant, which leads to:

$$\tilde{p}^{n+1} = \frac{\tau_{pt}^n}{\Delta t} \tilde{p}^n + \tau_{pt}^n R_p \quad (23)$$

with $\frac{1}{\tau_{pt}^n} = \frac{1}{\Delta t} + \frac{1}{\tau_p^n}$

The influence of this term has been discussed in literature. According to [38], this term is not required to get stability and convergence bounds for Stokes flow. However as noted in [24], for the Darcy problem, the pressure sub-grid scale cannot be neglected to satisfy the inf-sup conditions.

3.4. FE scale temporal discretisation

We remind that the FE scale problem reads as for linear element (see Equation (12)):

$$\begin{aligned} & \underbrace{(\partial_t \mathbf{u}_h, \mathbf{v}_h) + \nu(\nabla \mathbf{u}_h, \nabla \mathbf{v}_h) + \langle \mathbf{u}_h \cdot \nabla \mathbf{u}_h, \mathbf{v}_h \rangle - (p_h, \nabla \cdot \mathbf{v}_h) + \sigma \langle \mathbf{u}_h, \mathbf{v}_h \rangle - \langle \mathbf{f}, \mathbf{v}_h \rangle}_{\text{Galerkin part}} \\ & - \underbrace{(\tilde{\mathbf{u}}, a \cdot \nabla \mathbf{v}_h) + \langle \tilde{\mathbf{u}} \cdot \nabla \mathbf{u}_h, \mathbf{v}_h \rangle - (\tilde{p}, \nabla \cdot \mathbf{v}_h)}_{\text{Stabilization part}} = 0 \\ & (\partial_t p_h, q_h) + \zeta^{-1}(\nabla \cdot \mathbf{u}_h, q_h) - \zeta^{-1}(\tilde{\mathbf{u}}, \nabla q_h) = 0 \end{aligned} \quad (24)$$

The motivation of using an artificial compressibility method is the possibility to use an explicit time integration scheme of the flow equations [44]. This approach has been successfully used to solve Navier Stokes equations on binarised grayscale images [15]. Considering the Navier-Stokes-Brinkman equations, velocity varies from several orders of magnitude. To resolve this problem, a fully explicit numerical scheme will require very small time steps for numerical stability.

In this paper we adopt a splitting scheme: we consider the Navier-Stokes part fully explicitly, using a simple second order time integration scheme, and we consider the Darcy term $\sigma \mathbf{u}$ implicitly as a source term in the momentum equation in this framework. The Darcy term is linear which allow to treat it easily in a fully implicit way. This leads to a more robust description in comparison with a full explicit approach. Similar approach to consider the Darcy term as an implicit source term into the momentum equation has been used in [2,46] to improve stability.

We have for the momentum equation:

$$\begin{aligned} M \frac{\mathbf{u}_h^{n+1} - \mathbf{u}_h^n}{\Delta t} + M \sigma \mathbf{u}_h^{n+1} + R H S_u(\mathbf{u}_h^n, p_h^n) &= 0 \\ \mathbf{u}_h^{n+1} &= \frac{1}{1 + \sigma \Delta t} (\mathbf{u}_h^n - \Delta t M^{-1} R H S_u(\mathbf{u}_h^n, p_h^n)) \end{aligned} \quad (25)$$

where

$$\begin{aligned} R H S_u(\mathbf{u}_h^n, p_h^n) &= \nu(\nabla \mathbf{u}_h, \nabla \mathbf{v}_h) + \langle a \cdot \nabla \mathbf{u}_h, \mathbf{v}_h \rangle \\ &- \langle \tilde{\mathbf{u}}, a \cdot \nabla \mathbf{v}_h \rangle - (p_h, \nabla \cdot \mathbf{v}_h) - (\tilde{p}, \nabla \cdot \mathbf{v}_h) - \langle \mathbf{f}, \mathbf{v}_h \rangle \end{aligned} \quad (26)$$

M is the mass matrix defined as $M \mathbf{u}_h = (\mathbf{u}_h, \mathbf{v}_h)$, and we use the lumped approach to calculate M^{-1} .

Similarly, we have for the mass continuity equation:

$$\begin{aligned} M \frac{p_h^{n+1} - p_h^n}{\Delta t} + R H S_p(\mathbf{u}_h^n, p_h^n) &= 0 \\ p_h^{n+1} &= p_h^n - \Delta t M^{-1} R H S_p(\mathbf{u}_h^n, p_h^n) \end{aligned} \quad (27)$$

where

$$R H S_p(\mathbf{u}_h^n, p_h^n) = \zeta^{-1}(\nabla \cdot \mathbf{u}_h, q_h) - \zeta^{-1}(\tilde{\mathbf{u}}, \nabla q_h) \quad (28)$$

M is the mass matrix defined as $M p_h = (p_h, q_h)$, and we use the lumped approach to calculate M^{-1} .

Remark 1. There are different ways to build the mass lumping, but these methods are the same while using Cartesian grids and bi-linear element. It is known that the simple lumping approach will introduce dispersion effect [47–50]. For further work, we could easily modify the mass lumping approach for transient calculations, using for example the approach proposed in [50].

Remark 2. We use first order time integration for modelling the sub-grid scales. This is consistent since the sub-grid scales are multiplied by the stabilisation parameters, which are of the order of the time step size. Note that they essentially behave as the critical time step that would be found in a forward Euler time integration.

3.5. Algorithm

The solver has been implemented using FORTRAN 90 and integrated in Python framework. The code has been parallelised using hybrid OpenMP/MPI. This parallelisation approach has been widely used and has demonstrated its efficiency [51–53]. MPI for Python package mpi4py is used for its simplicity, efficient high-level data structures and effective approach to object-oriented programming with dynamic typing and dynamic binding. It supports modules and packages, which encourages program modularity and code reuse on most platforms. Besides Python codes are quickly developed, easily maintained, and can achieve a high degree of integration with other libraries written in compiled languages, such as FORTRAN.

The parallelisation is achieved by decomposing the whole computational domain on different subdomains, allocating each of these subdomains to computation resources and solving the problem (computing the flow) independently on these subdomains.

Algorithm 1 Massively parallel stabilised FE solver for Navier-Stokes-Brinkman system.

- Domain decomposition and initialisation of MPI communications
 - Initialisation of the lumped mass matrix, porosity and permeability matrices
 - Read \mathbf{u}_h^0, p_h^0 and set $\tilde{\mathbf{u}} = 0$ and $\tilde{p} = 0$
 - Loop over time step n until steady state convergence is reached:
 - Loop over elements, loop over integration points:
 - Evaluate velocity prediction $\hat{\mathbf{u}}_h^{n+1}$ and pressure prediction \hat{p}_h^{n+1} at time step n+1 using the second order approximation:

$$\hat{\mathbf{u}}_h^{n+1} = \frac{3}{2} \hat{\mathbf{u}}_h^n - \frac{1}{2} \hat{\mathbf{u}}_h^{n-1}, \quad \hat{p}_h^{n+1} = \frac{3}{2} \hat{p}_h^n - \frac{1}{2} \hat{p}_h^{n-1}$$
 - Calculate the stabilisation parameters τ_{ut}^n, τ_{pt}^n as in (16), (23) and the residuals \mathbf{R}_u^n, R_p^n as in (14).
 - Evaluate velocity and pressure sub-grid scales:

$$\tilde{\mathbf{u}}^{n+1} = \frac{\tau_{ut}}{\Delta t} \hat{\mathbf{u}}^n - \tau_{ut} \mathbf{R}_u^n, \quad \tilde{p}^{n+1} = \frac{\tau_{pt}}{\Delta t} \hat{p}^n - \tau_{pt} R_p^n$$
 - Solve unknown variables for time step n+1 for all test functions \mathbf{v}_h and q_h :

$$\begin{aligned} * \text{ } RHS_u^n &= (a \cdot \nabla \hat{\mathbf{u}}_h^{n+1}, \mathbf{v}_h) + \nu (\nabla \hat{\mathbf{u}}_h^{n+1}, \nabla \mathbf{v}_h) - (\hat{p}_h^{n+1}, \nabla \cdot \mathbf{v}_h) - (\tilde{p}^n, \nabla \cdot \mathbf{v}_h) - (\hat{\mathbf{u}}^n, a \cdot \nabla \mathbf{v}_h) - (\mathbf{f}, \mathbf{v}_h) \\ * \text{ } RHS_p^n &= \zeta^{-1} (\nabla \cdot \hat{\mathbf{u}}_h^{n+1}, q_h) - \zeta^{-1} (\hat{\mathbf{u}}^n, \nabla q_h) \end{aligned}$$
 - MPI communications and addition of the neighbour integration value to FE nodes
 - Update the velocity and pressure for the next time step n+1:

$$\begin{aligned} * \text{ } (\mathbf{u}_h^{n+1}, \mathbf{v}_h) &= \frac{1}{1+\sigma \Delta t} ((\mathbf{u}_h^n, \mathbf{v}_h) - \Delta t RHS_u^n) \\ * \text{ } (q_h, p_h^{n+1}) &= (q_h, p_h^n) - \Delta t RHS_p^n \end{aligned}$$
 - Prescribe boundary conditions:
 - $\mathbf{u}_h^{n+1} = \bar{\mathbf{u}}$ on $\partial\Omega_u$, $p_h^{n+1} = \bar{p}$ on $\partial\Omega_p$
-

4. Numerical validation

This section is dedicated to validate the proposed algorithm. The choice of the stabilisation parameter will change the stability and accuracy of the solution. Therefore, in the following section, we study the sensitivity of the mesh resolution and the stabilisation parameter on the velocity and pressure field computed to determine the mesh resolution and the optimal stabilisation parameter that allow to minimise numerical errors. A particular attention is drawn to the behaviour of the method near interface. The accuracy of the velocity and pressure field is assessed. For all these following cases, the viscosity was taken to $\nu = 1 \times 10^{-6} \text{ m}^2 \cdot \text{s}^{-1}$. The time step was $dt = \frac{h}{12\nu}$. The code was run until the flow reached the steady state. In their previous work, [44] set the value of c_1 (stabilisation parameter for Stokes flow) at 4. Given their numerical results, we used this value for all the following cases. Concerning the stabilisation parameter c_3 for Darcy flow, the optimal value has been discussed below in the one dimensional uniform flow case.

4.1. One dimensional uniform flow

The first problem considered is one dimensional uniform flow. This case allows to validate the numerical method for the accurate computation and the stability of the computed velocity and pressure field. The computational domain (see Fig. 1) was 0.05 mm wide and 0.3 mm long. The domain is divided into three equal parts: a left fluid domain, a middle porous domain I, and a right porous domain II. The porous domains I and II were assumed to possess a porosity of 0.9 and 0.8 and micro-permeability of $1 \times 10^{-11} \text{ m}^2$ and $2 \times 10^{-12} \text{ m}^2$, respectively. As the boundary conditions, the inflow velocity of 0.001m/s was given to the left side and the pressure on the right side was kept at 0. The free-slip condition was imposed on the top and bottom of the domain. The flow velocity and the pressure were set at zero in the domain.

In order to study the influence of stabilisation parameter, velocity and pressure distributions along the channel have been computed using a grid 240×40 (leading to a cell length 1.25×10^{-6}), for different values of the stabilisation parameter c_3 . These computed distributions are compared with analytical solution in Figs. 2 and 3. For the velocity field analytical solution

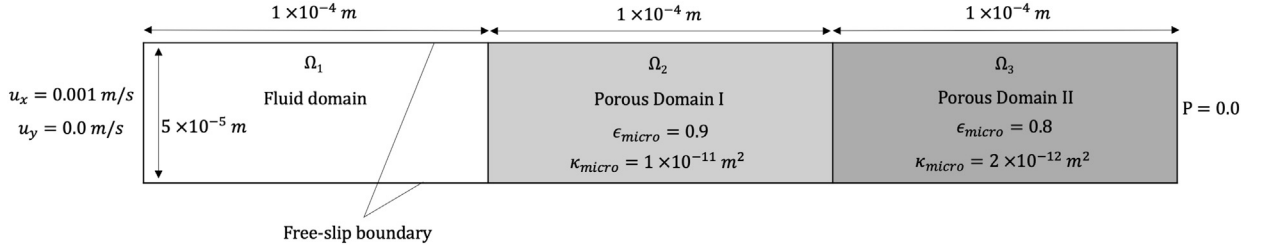


Fig. 1. Geometry and boundary conditions for one-dimensional uniform flow.

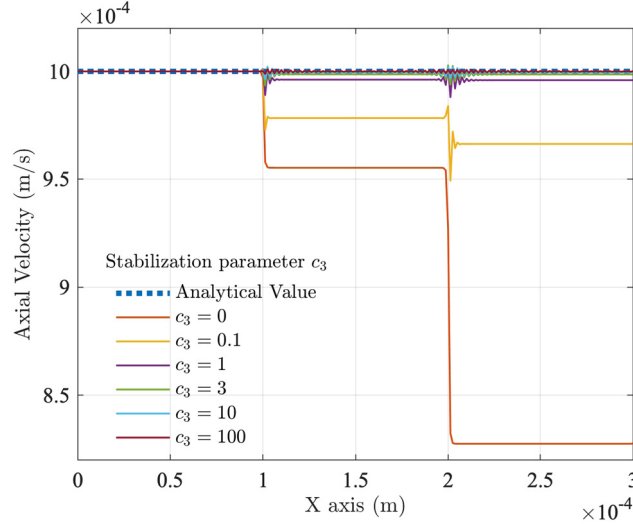


Fig. 2. Influence of stabilisation parameter c_3 on the computed velocity distribution along the channel for a grid 240×40 , $h = 1.25 \times 10^{-6}$ m. (For interpretation of the colours in the figure(s), the reader is referred to the web version of this article.)

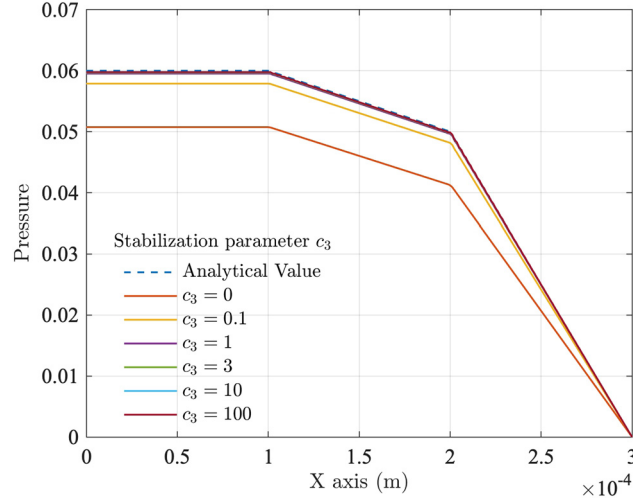


Fig. 3. Influence of stabilisation parameter c_3 on the computed pressure distribution along the channel for a grid 240×40 , $h = 1.25 \times 10^{-6}$ m.

corresponds to the constant velocity imposed at the inlet, for the pressure field, the analytical pressure is computed using the Darcy's Law.

Figs. 2 and 3 show the importance of the stabilisation parameter. For this case, if the stabilisation parameter τ_d is neglected ($c_3 = 0$), the velocity distribution shows a variation of 20 % from analytical value. The bigger the stabilisation parameter c_3 is, more accurate is the velocity distribution, but the velocity distribution oscillates on a longer distance from interface. The pressure field is less sensible to the stabilisation parameter used. Fig. 3 shows that pressure distribution is

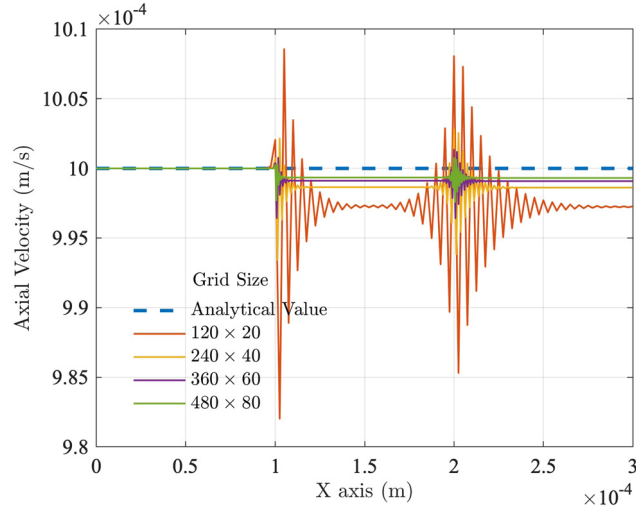


Fig. 4. Influence of grid size on the computed velocity distribution along the channel for stabilisation parameter $c_3 = 3$.

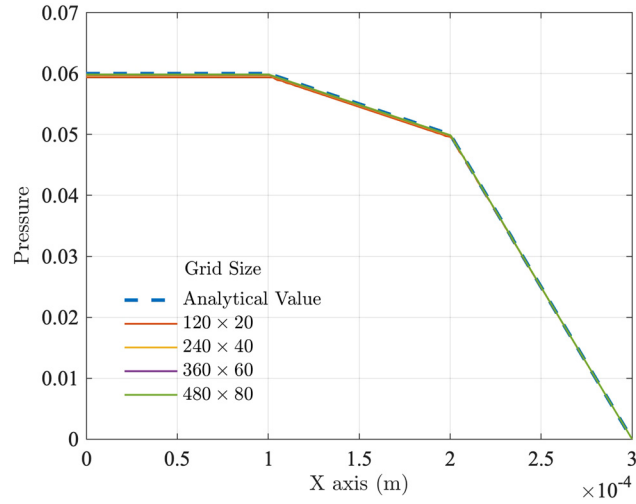


Fig. 5. Influence of grid size on the computed pressure distribution along the channel for stabilisation parameter $c_3 = 3$.

stable and agreed fairly well with the prediction by Darcy's law for stabilisation parameter c_3 higher than 1. A stabilisation parameter $c_3 = 3$ seems to be a good compromise between the accuracy and stability of velocity field.

In order to study the influence of the mesh resolution, velocity and pressure distribution along the channel have been computed using a stabilisation parameter $c_3 = 3$, for different grid sizes. These computed distributions are compared with analytical solution for velocity and pressure field in Figs. 4 and 5.

As shown Fig. 4 numerical error decrease with the increase of mesh resolution. A finer mesh enough is able to limit the maximum error at less to 0.5% as shown Fig. 6.

The pressure field is less sensible to the mesh size. Fig. 5 shows that pressure distribution is stable and agreed fairly well with the prediction by Darcy's law even for coarse mesh.

To complete this study we perform a convergence study with the mesh refinement. This allows to determine also the order of convergence reached by the method implemented. To do this we compare the results obtained using different mesh size with the fields given by the analytical expression.

To measure the error, we choose the L^2 norm approximated by the discrete expression (29):

$$\text{Error} = \|Y_{\text{theoretical}} - Y_{\text{computed}}\|_2 = \sqrt{\sum_{i=1}^N (y_{i,\text{theoretical}} - y_{i,\text{computed}})^2} \quad (29)$$

where $Y_{\text{theoretical}}$ represents the analytical result. Fig. 7 shows the error of the computed velocity with the number of elements in the mesh in the X direction computed with (29).

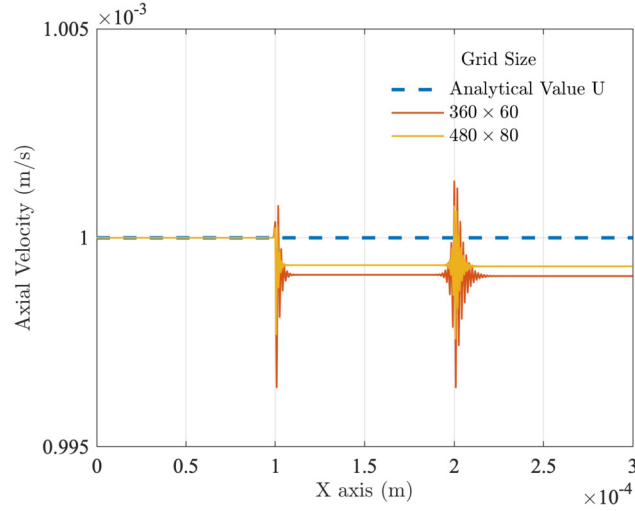


Fig. 6. Influence of grid size on the computed velocity distribution along the channel for stabilisation parameter $c_3 = 3$.

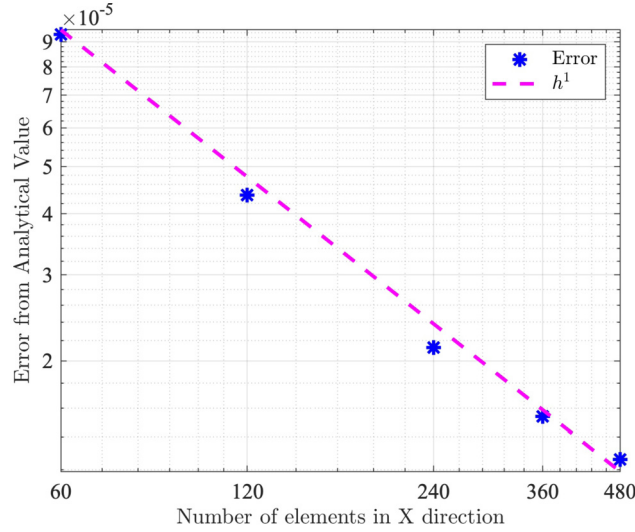


Fig. 7. Velocity Error from Analytical Value (L^2 norm) in Log-Scale.

As mentioned in [15], using the stabilised formulation with equal-order tri-linear elements, the error of the velocity gradient and pressure in the L^2 -norm is expected to decrease linearly with the element size, which suggests a 2^{nd} order convergence of the velocity with the L^2 norm if the solution is smooth. However Fig. 7 suggests a first order convergence of the velocity with the L^2 norm. Then we considered a numerical experiment for Stokes-Brinkman flow with smooth solutions to check the theoretical convergence rates presented in [21]. The problem with exact solutions:

$$\mathbf{u} = (2\pi \sin(2\pi x) \cos(2\pi y), -2\pi \cos(2\pi x) \cos(2\pi y)), \quad p = \cos(2\pi x) \cos(2\pi y - 1) \quad (30)$$

where the free Stokes flow in region $\Omega^S \equiv (0, 1) \times (0.5, 1)$ and Darcy flow in region $\Omega^D \equiv (0, 1) \times (0, 0.5)$. The whole velocity is enforced on Stokes boundary region and only normal component is constrained on Darcy region. The method shows a second order of convergence for Q1-Q1 pair.

Applied to micro-CT images, this case shows the importance of the micro-CT images resolution. A resolution not enough small will lead to instability field in heterogeneous regions, with high variations in the micro-permeability field. As explained by [19], the transition zone at the interface regions is estimated to be of the order of $\sqrt{\kappa_{\text{micro}}}$. This value can be a criterion to choose the appropriate resolution to resolve this transition zone and minimise the instabilities. Thus a computational grid fine enough is required to resolve this transition zone. For example, if the micro-porosity field κ_{micro} is distributed around $1 \times 10^{-12} \text{ m}^2$, we can think that a suitable cell length will be of the order of $\sqrt{\kappa_{\text{micro}}} = 1 \times 10^{-6} \text{ m}$. Given the results obtained for this case, a stabilisation parameter $c_3 = 3$ will be used in the following cases.

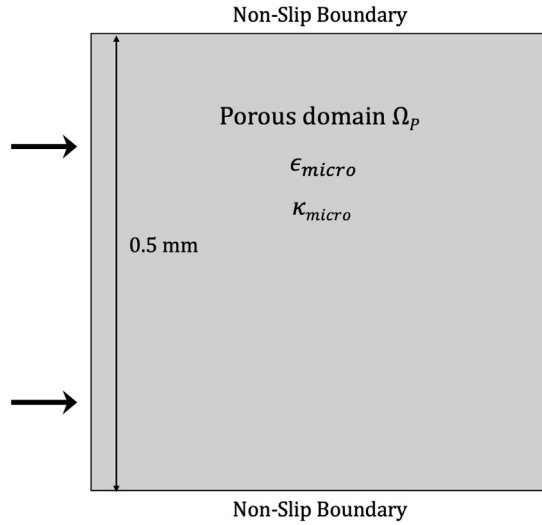


Fig. 8. Geometry and Boundary conditions.

4.2. Identification of Darcy-Brinkman, Stokes and transition regions

This case allows to determine for which micro-permeability κ_{micro} , either Stokes part or Darcy Part is dominant, by comparing the effective permeability k_{eff} computed in a channel filled with a homogeneous porous medium with Stokes and Darcy permeability.

The computational domain, presented in Fig. 8, was 0.5 mm square. Non-slip boundary conditions were applied on the top and bottom wall. The flow was moved by a body force taken to 1. The channel was filled with homogeneous porous media of micro porosity ϵ_{micro} and micro permeability κ_{micro} . An uniform grid 100×100 was used for the computation.

To compute k_{eff} , we compute the specific discharge through the boundary at $x = L$ as:

$$q = \frac{1}{L} \int_0^L u_x dy \quad (31)$$

Then, the effective permeability k_{eff} of the domain can be obtained from Darcy's law:

$$k_{\text{eff}} = -\frac{q\mu}{\nabla p} \quad (32)$$

where q is the discharge coefficient, μ the dynamic viscosity and ∇p the pressure gradient applied along the domain. For high permeability porous media we are in case of Stokes flow. This setup corresponds thus to the 2D Poiseuille flow in a channel, for which the effective permeability is given by [16]:

$$k_{\text{eff}} = k_s = \frac{L^2}{12} \quad (33)$$

where k_s is the Stokes permeability.

For low permeability porous media, we are in Darcy regime, for which the effective permeability is expected to be [16]:

$$k_{\text{eff}} = \kappa_{\text{micro}} \quad (34)$$

Fig. 9 presents the effective permeability k_{eff} computed in the channel for porous media of different micro-permeability κ_{micro} . It shows that the proposed method is able to deal with either Stokes or Darcy flow with any distinction. It can be seen that we are Darcy regime for porous media whose micro-permeability κ_{micro} is less than $1 \times 10^{-9} \text{ m}^2$. The proposed method allows to capture the effect of high permeability as well as low permeability region.

This simple case can be a criterion for the three-phase segmentation of a micro-CT images (see Section 5). Indeed, taking for example the Fig. 9, for micro-permeability κ_{micro} equal to 10^{-8} m^2 we are still in Stokes regime. Thus micro-porous regions with higher permeability can be considered as pore-space with an infinite permeability.

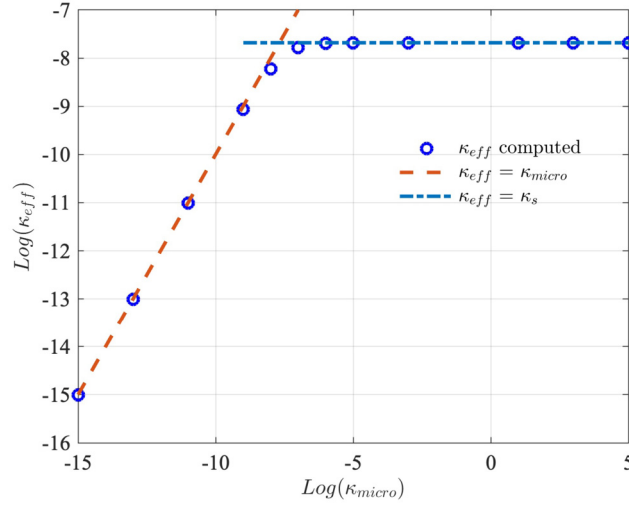


Fig. 9. Computed effective permeability according to micro permeability κ_{micro} .

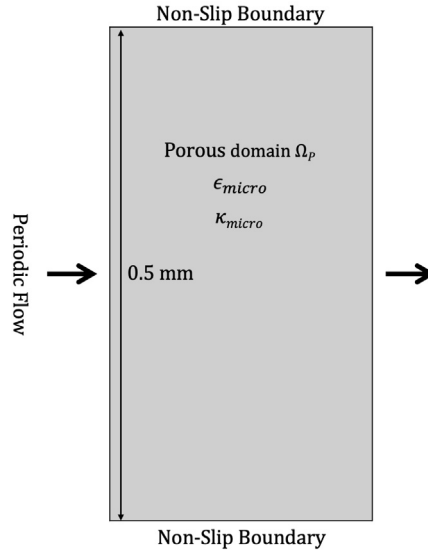


Fig. 10. Geometry and boundary conditions for channel flow in Porous media.

4.3. Bounded 2D channel validation

Here we compare the proposed model with analytic solutions of Stokes–Brinkman equations (Equation (1)). It is a bounded 2D channel filled with homogeneous porous media. The computational domain (see Fig. 10) was 0.5 mm wide and 0.1 mm long and consists of 2000 cells (100×20). The domain is periodic along the X axis, and non-slip boundary conditions are applied on the top and bottom of the channel. The flow is driven by a fixed body force of $(F_x, 0, 0)$ where $F_x = 1$. The domain is filled with a porous medium with a porosity ϵ_{micro} and a micro-permeability κ_{micro} .

Analytical velocity profile is derived from Stokes–Brinkman equation, considering $u(y = 0) = u(y = L) = 0$ as boundary condition.

When the channel is filled with a homogeneous porous medium, in Darcy regime, analytical velocity is given by [19]:

$$u = \left(e^{-\sqrt{\frac{\epsilon_{\text{micro}}}{\kappa_{\text{micro}}}} y} - 1 \right) \frac{\kappa_{\text{micro}}}{\mu} \nabla p \quad (35)$$

where ∇p in the pressure gradient through the porous media.

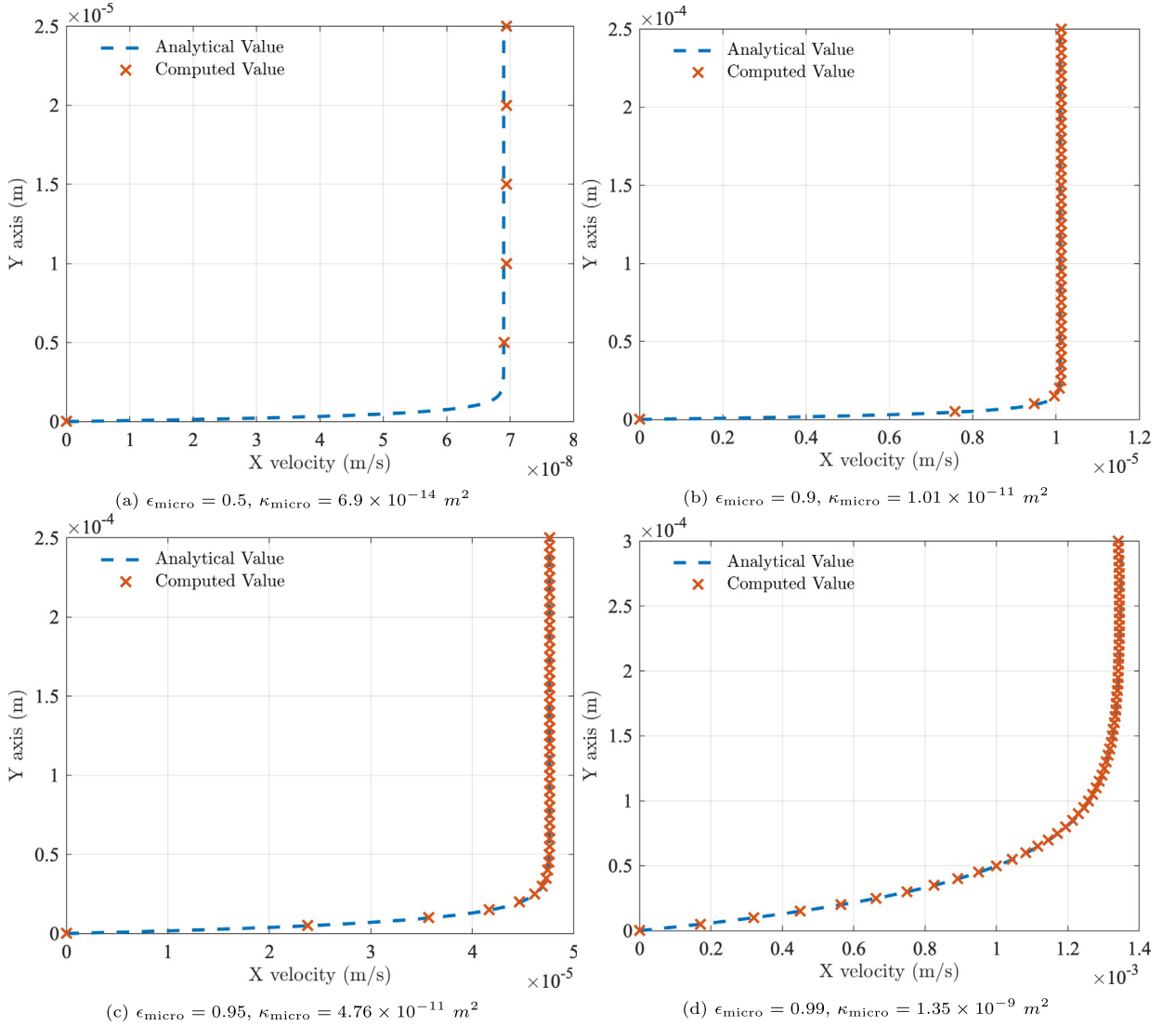


Fig. 11. Velocity profiles along Y axis compared with analytical value.

In case of free flow ($\epsilon_{\text{micro}} = 1$ and $\kappa_{\text{micro}} = \infty$) the velocity field corresponds to Poiseuille velocity, given by:

$$u = \frac{L^2}{8\mu} \nabla P \left(\frac{4y}{L} - \frac{4y^2}{L^2} \right) \quad (36)$$

The flow was computed in homogeneous porous media with different micro-permeability κ_{micro} . The velocity profiles obtained along the Y axis are compared with analytical results in Figs. 11 and 12.

It can be seen that the proposed method matches very well with analytical solution in both Darcy-Brinkman flow and Stokes flow. Especially, the velocity near the wall, region with high gradient of velocity, is represented accurately. For low permeability, the velocity gradient is important near the wall, thus a finer mesh is needed to catch this high variation.

4.4. Poiseuille flow over a porous media

In this case we consider now a Poiseuille flow in a fluid domain over the porous medium, in which the fluid is driven horizontally in both the fluid domain and the porous medium with a horizontal pressure gradient. This case shows the model ability to deal with both Navier-Stokes flow at fluid nodes and Darcy-Brinkman flow at gray nodes uniformly. The main interest of this case is to analyse how the code deals with the velocity at the interface between porous and fluid domain. Velocity profile along the Y axis is compared with analytical value. The computational domain was 1 mm wide and

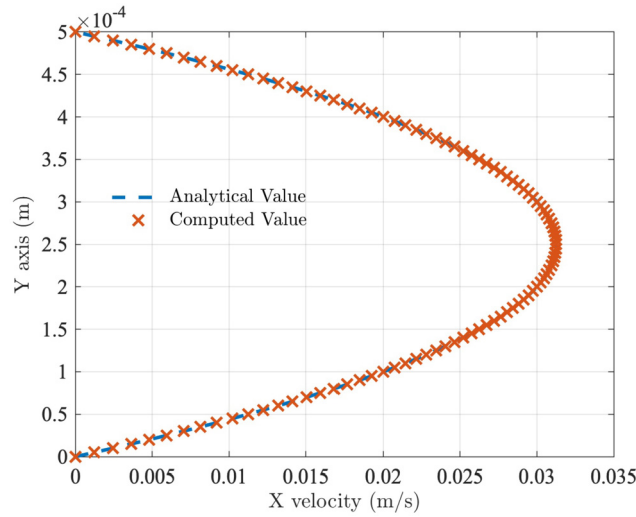


Fig. 12. Velocity profile along Y axis for $\epsilon_{\text{micro}} = 1$ and $\kappa_{\text{micro}} = \infty$, compared with Poiseuille Velocity.

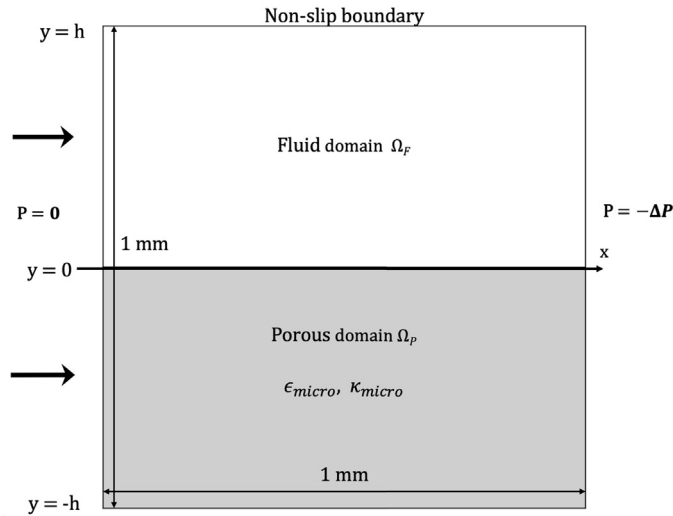


Fig. 13. Geometry and boundary conditions for Poiseuille flow over porous media.

long (see Fig. 13). Non-slip boundary conditions are applied on the top. The flow is driven by a pressure gradient taken to -1. We call U_f and U_p the velocities in the fluid domain Ω_F and in porous domain Ω_P respectively.

For this case, where $U_f(y = h) = 0$ and $U_f(y = 0) = U_p(y = 0)$, velocities in fluid and porous domain are given by [19]:

$$U_f = \frac{\nabla p}{2\mu} \left(y + h + \frac{-h^2 + 2\kappa_{\text{micro}}}{h + \sqrt{\frac{\kappa_{\text{micro}}}{\epsilon_{\text{micro}}}}} \right) (y - h) \quad \text{in } \Omega_F \quad (37)$$

$$U_p = \frac{\nabla p}{2\mu} \frac{-h^2 + 2\kappa_{\text{micro}}}{h + \sqrt{\frac{\kappa_{\text{micro}}}{\epsilon_{\text{micro}}}}} \sqrt{\frac{\kappa_{\text{micro}}}{\epsilon_{\text{micro}}}} e^{\sqrt{\frac{\epsilon_{\text{micro}}}{\kappa_{\text{micro}}}} y} - \frac{\kappa_{\text{micro}}}{\mu} \nabla p \quad \text{in } \Omega_P \quad (38)$$

where ∇p is the pressure gradient in the domain. Analytical solution was established by using the Beavers-Joseph condition on interface Fluid/Porous domain, which describes the velocity profile at the interface as:

$$\frac{du}{dy} = \frac{\alpha}{\kappa_{\text{micro}}} (U_f - U_p) \quad (39)$$

where α is a constant which depends on the porous medium (here α was taken as $\alpha = \sqrt{\epsilon_{\text{micro}}}$). A mesh convergence analysis has been performed using a porous medium which is assumed to have a micro-porosity $\epsilon_{\text{micro}} = 0.99$ and a micro-permeability $\kappa_{\text{micro}} = 1 \times 10^{-9} \text{ m}^2$. The code is run until the flow reached the steady state.

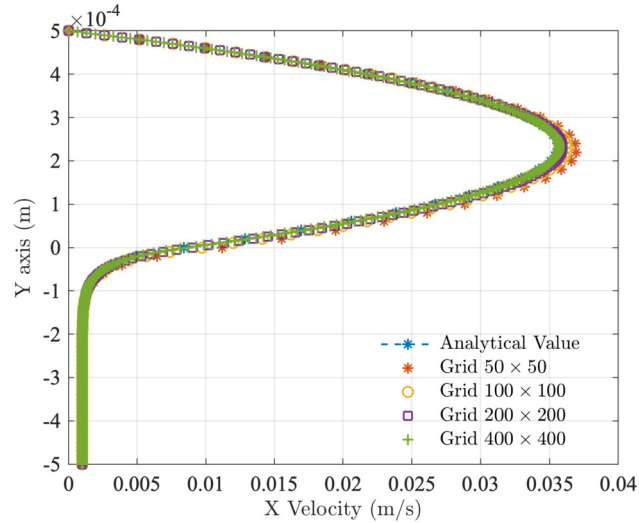


Fig. 14. Velocity profile for different grid, $\kappa_{\text{micro}} = 1e - 9 \text{ m}^2$, $\epsilon_{\text{micro}} = 0.99$.

Fig. 14 shows the velocity profiles along Y axis for different grid size. It can be seen that the results become mesh independent for enough fine mesh.

Velocity profiles have been computed using a grid 400×400 for different porous medium. Results are presented in Fig. 15.

This figure emphasises the continuity of the tangential velocity at the interface between porous and fluid domain, for different magnitude of micro permeability κ_{micro} . It shows also the ability of the code to deal with Stokes or Darcy flow without any distinction.

4.5. 2D cavity lid driven flow

The problem considered here is the well documented benchmark case of the lid-driven cavity flow to test the proposed method and the implementation in 2D. A porous domain is placed at the bottom of the cavity to allow the analysis of the coupled flows in porous and fluid domains. Velocity profiles at $x/L = 0.5$ and at $y/L = 0.5$ are compared with the numerical results obtained [54].

A scheme of the test problem configuration is shown in Fig. 16. The computational domain was 1 mm square and the top wall moving to the right at a velocity $u_x = 0.1 \text{ m.s}^{-1}$, leading to a Reynolds Number of $Re = 100$. The bottom and two vertical walls are non-slip boundaries. A 200×200 uniform mesh was used for computation.

Fig. 17 compares velocity profiles in the cavity (without porous media) with results given by [55]. We can see that the velocity profiles computed in the cavity are in good agreement with data proposed by [55].

Figs. 18 and 19 present velocity vectors and streamlines, and pressure distribution in the cavity for different positions of the fluid-porous interface. It can be seen the behaviour of the flow at the interface fluid/porous media and how the flow develops in the porous media.

These different cases show the strong ability of the code to deal with Stokes and Darcy-Brinkman flow indifferently and that the same formulation works for the Stokes and the Darcy problems. These tests show also the behaviour of the velocity distribution in cases where interface is tangential or normal to the flow direction. As discussed above, the use of the right stabilisation parameter and a sufficient mesh resolution allow to ensure the right behaviour of the velocity distribution. The pressure distribution computed is less sensible to these parameters, and shows a strong stability and accuracy.

5. 3D grayscale simulations: materials, methods and result

Digital Rock Physics (DRP) uses the absorption of X-ray to obtain 3D grayscale micro-CT images. Each 'voxel' value corresponds to a measure of linear-absorption coefficients, which for a porous medium depends on the porosity and the composition of the solid matrix.

The samples used in this work were found in [56] which contains a set of 11 sandstone plugs from Kocurek Industries: Bandera Gray, Parker, Kirby, Bandera Brown, Berea Sister Gray, Berea Upper Gray, Berea, Castlegate, Buff Berea, Leopard and Bentheimer. In this work, we use a Berea sandstone sample obtained from a larger block. The cylindrical sample (height = 30 mm, radius = 5 mm) was obtained by using high-resolution 3D X-ray microtomography. The image processing is explained in [57].

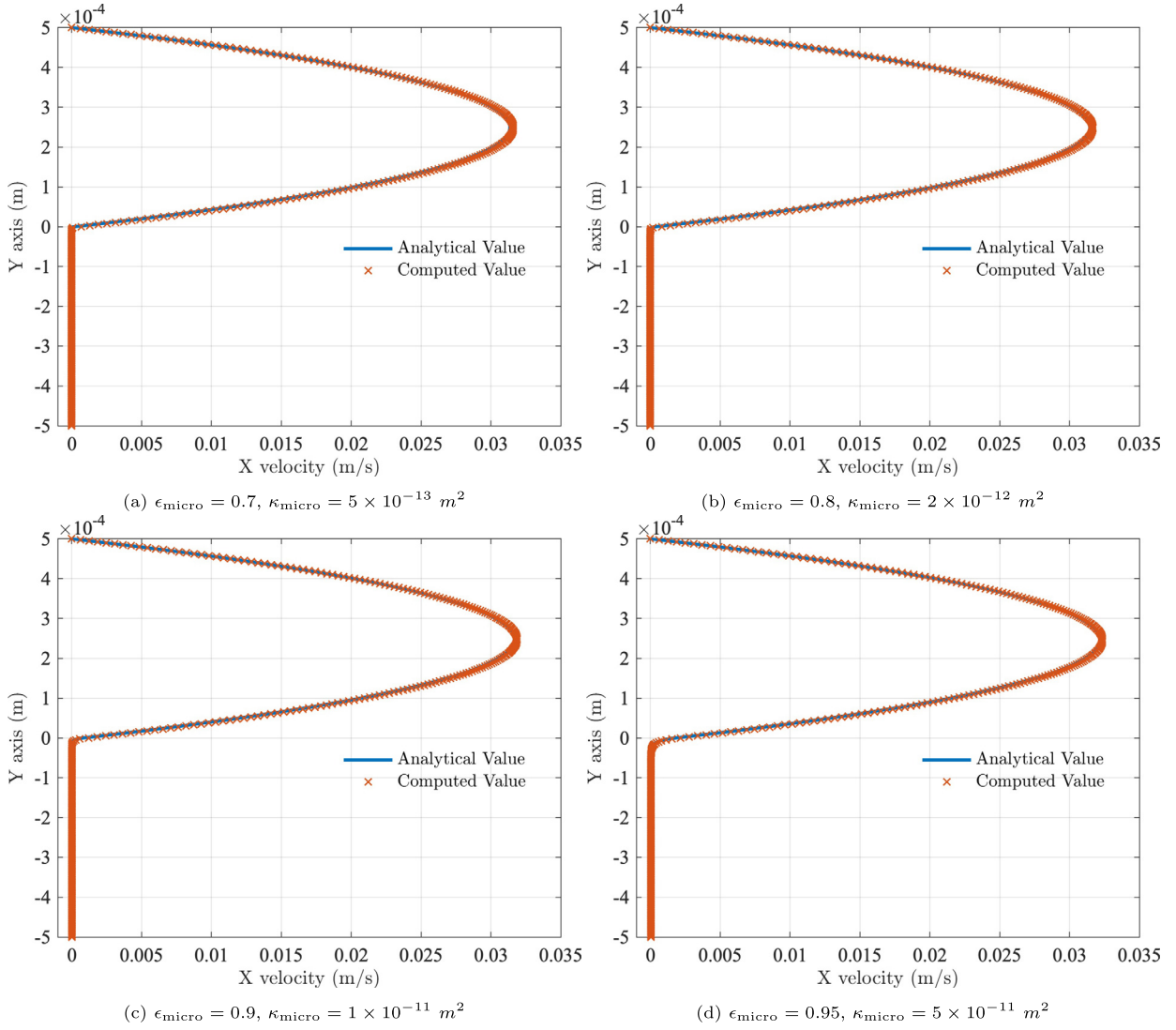


Fig. 15. Velocity profiles along Y axis compared with analytical values.

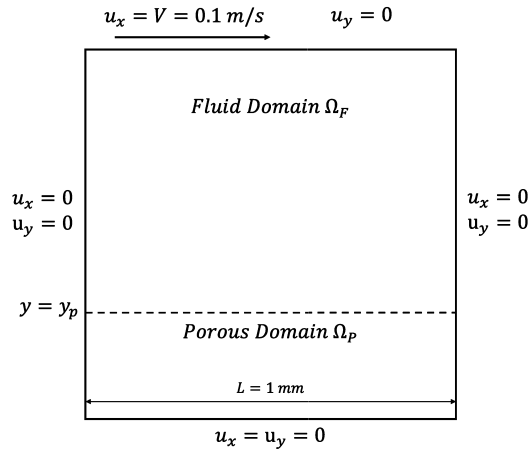


Fig. 16. Geometry and Boundary condition for Cavity flow.

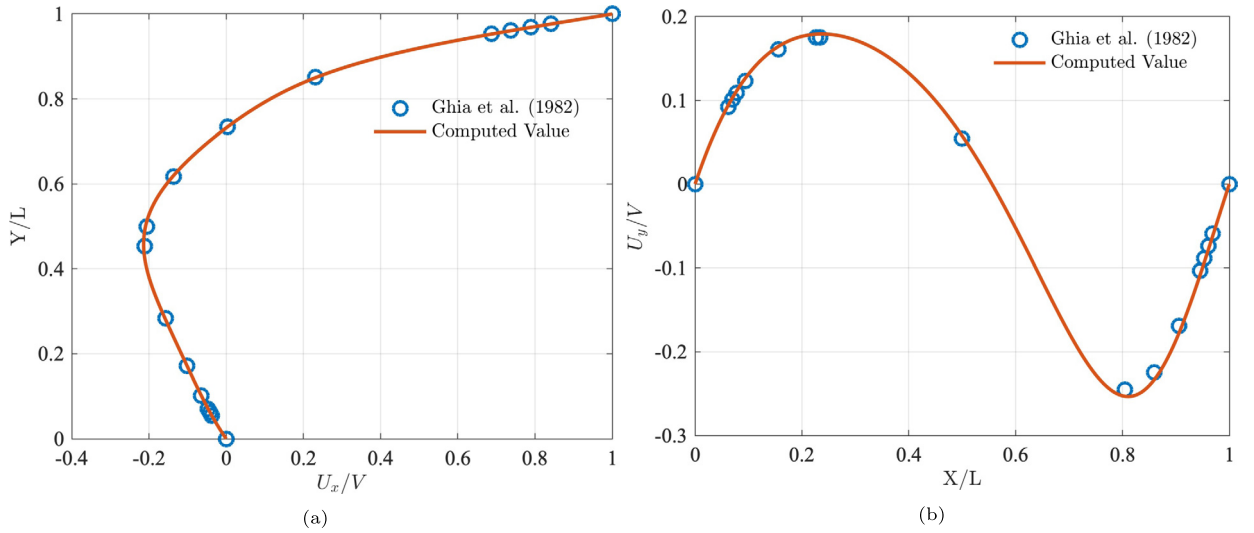


Fig. 17. Computed flow velocity at cross sections of $y/L = 0.5$ and $x/L = 0.5$, $Re = 100$.

Step 1: The micro-CT images were divided into subsets containing 1000^3 cubic voxels and converted from 16-bit to 8-bit grayscale. An enhancement filter to equalise the contrast across multiple images have been applied. For each data set, the cumulative sum of grey level intensity were plotted. Only the grayscale level for which the cumulative histogram is under 99.8% were considered and mapped the remaining grayscale levels to the $[0, 255]$ interval.

Step 2: To reduce image noise, on each data set a 3D non-local means filter were executed using a smoothing factor of 1 and automatically estimated sigma parameters.

Step 3: With the filtered grayscale image, we perform a three-phase segmentation approach to identify the micro-porous phase by using two threshold I_p and I_s :

- if $0 \leq \text{Grayscale} \leq I_p$ we consider pore space
- if $I_p < \text{Grayscale} < I_s$ we consider microporous region
- if $I_s \leq \text{Grayscale} \leq 255$ we consider solid space

The threshold values have to be chosen carefully, since better spatial resolution and variations in the threshold value for binarisation have been reported to change the estimated permeability significantly [58]. Two algorithms, multi-level Otsu algorithm and two step watershed algorithm, were proposed to determine these threshold values [59]. Kang et al. [58] proposed a procedure based on gray-level histogram of the micro-CT images and the experimentally measured power spectral density (PSD). Soulaïne et al. [2] used the iterative growing-region algorithm to find these two thresholds. Sok et al. [60] used active contour method to perform this segmentation. Noiriel et al. [61] mentioned that for a bi-modal histogram, such as presented in Fig. 20, a good estimation of I_p is the arithmetic mean of the two values for which frequency is maximum. However they noted that better estimates of the threshold values are obtained by visual inspection. There are no clear guidelines for choosing a threshold. Although is a practical way to use histogram to find threshold values, often visual inspection combined with user experience and expertise is a more robust technique.

In this work, I_s was calculated by using the Isodata method available in Fiji, which led to $I_s = 59$ for the sample considered. I_p was found using visual inspection of the image slices on Fiji, which led to $I_p = 49$. Finally, the fractions of the different phases are: 74.65%, 21.78%, and 3.57% for the solid, macro-porosity, and micro-porous phases respectively. Soulaïne et al. [2] used a Berea sandstone found similar values for the three phases.

Micro-porosity field

Once the three phases segmentation is completed, the solid structure is mapped by the micro-porosity field, ϵ_{micro} , which varies between 0 to 1 and corresponds to the void fraction in each voxel. If $\epsilon_{\text{micro}} = 1$, the voxel contains void only, if $\epsilon_{\text{micro}} = 0$, the cell is entirely composed of solid mineral. Intermediate values ($0 < \epsilon_{\text{micro}} < 1$) denote micro-porous regions whose characteristic length scale is below the voxel size [2]. The micro-porosity field is mapped as followed,

$$\epsilon_{\text{micro}} = \begin{cases} 1 & I \leq I_p & \text{(apparent pore voxel)} \\ \frac{I_s - I}{I_s - I_p} & I_p < I < I_s & \text{(gray voxel)} \\ 0 & I \geq I_s & \text{(apparent solid voxel)} \end{cases} \quad (40)$$

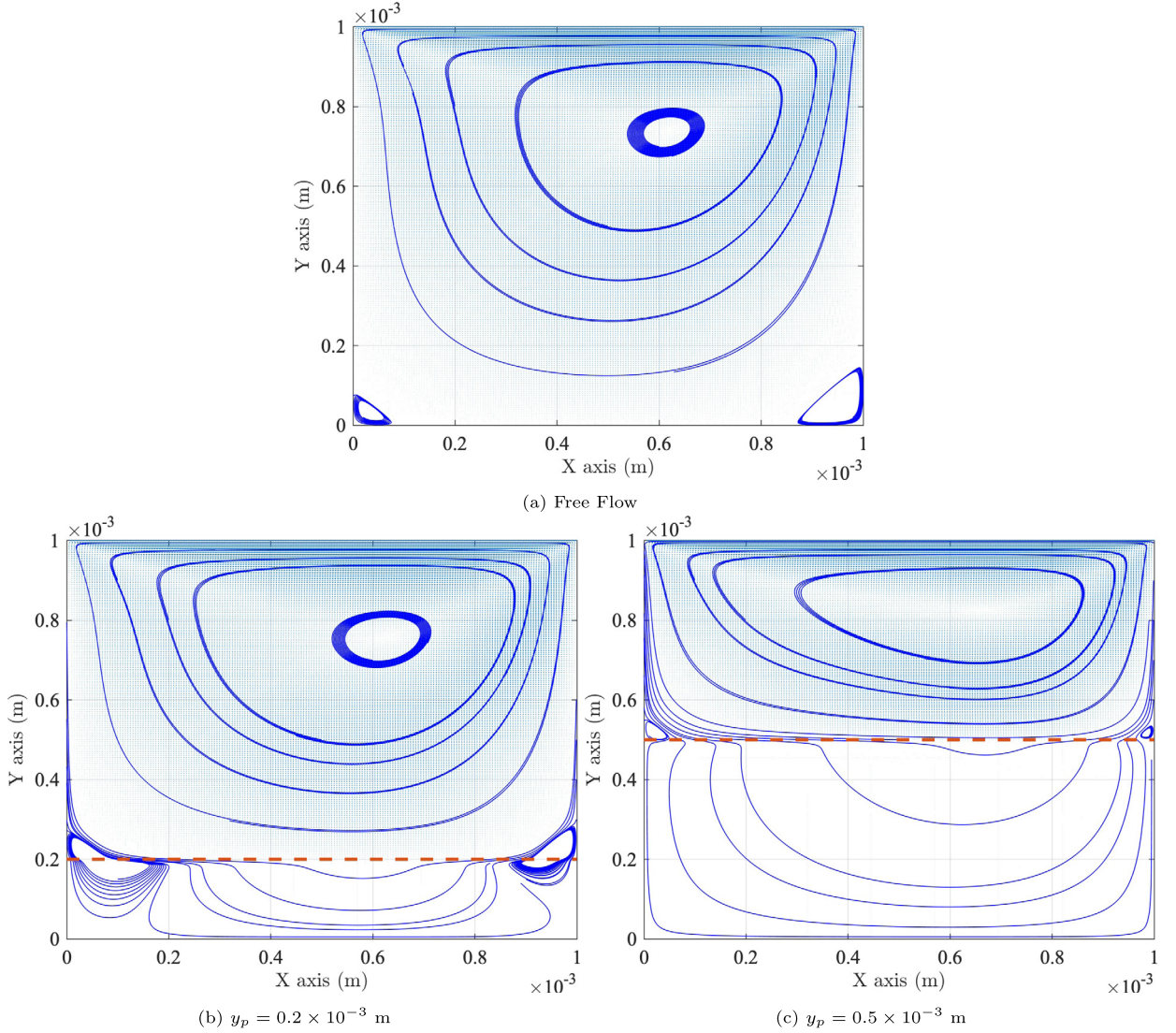


Fig. 18. Velocity vectors and streamlines in the cavity for different positions of the fluid-porous interface, $Re = 100$, Porous media, $\epsilon_{\text{micro}} = 0.9$, $\kappa_{\text{micro}} = 1 \times 10^{-11} \text{ m}^2$).

with I the grayscale intensity.

Relation between porosity and permeability

From the micro-porosity field ϵ_{micro} , the micro-permeability field κ_{micro} can be calculated. One of the most well known relations between micro-porosity ϵ_{micro} and micro-permeability κ_{micro} is the Kozeny-Carman (KC) relation [2,58] which estimates the micro-permeability κ_{micro} as,

$$\kappa_{\text{micro}}^{-1} = \frac{180}{d^2} \frac{(1 - \epsilon_{\text{micro}})^2}{\epsilon_{\text{micro}}^3} \quad (41)$$

where d is the characteristic length, which presents the grain size. This relation serves as an appropriate model since verifies relation (3). In the absence of additional information, d is associated with the voxel size.

Mesh generation

In the proposed model, the mesh derives naturally from the micro-CT images. A cell of the uniform computational grid corresponds to a voxel of the micro-CT images. Thus, the cell length is imposed by the micro-CT images resolution. Given

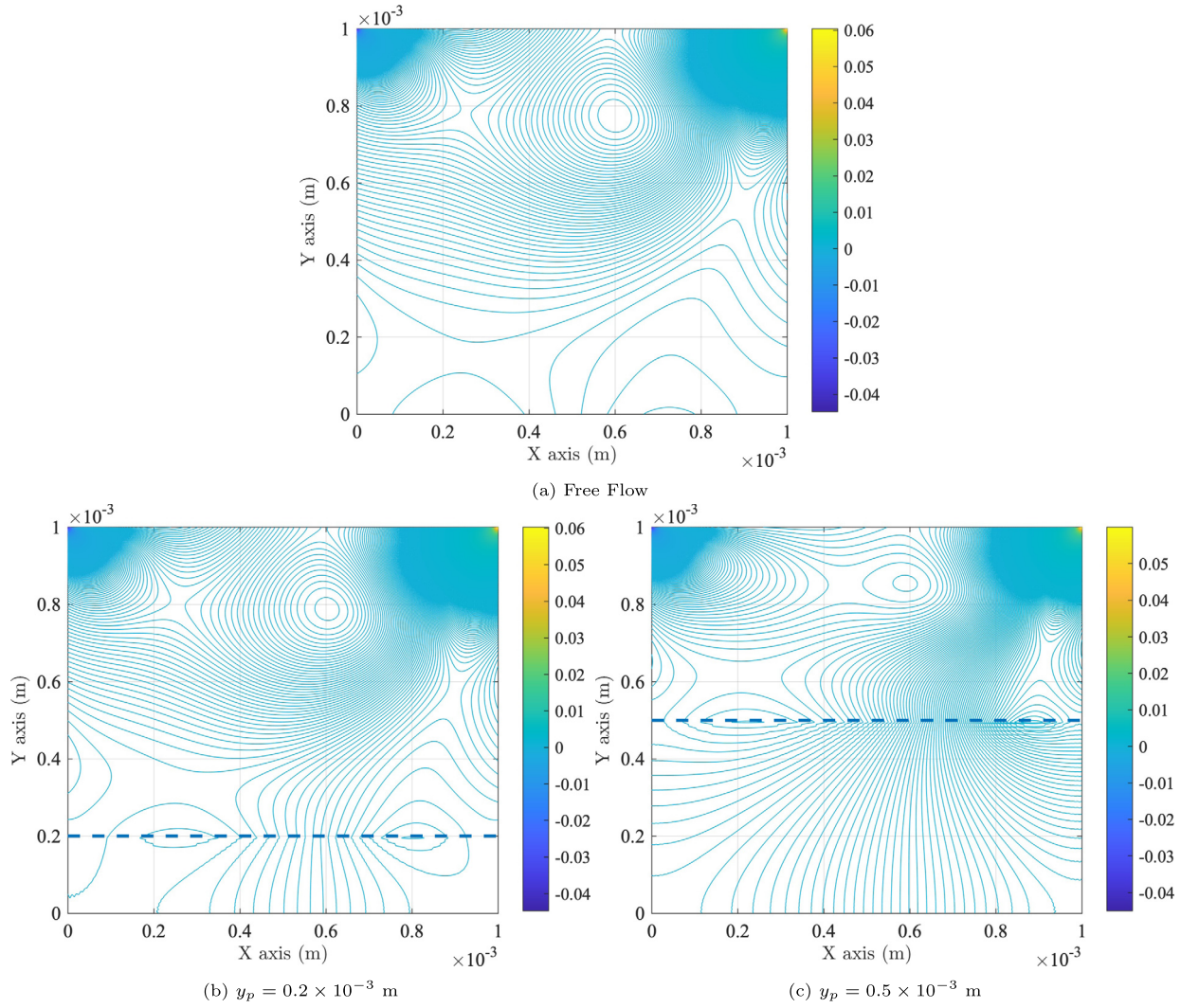


Fig. 19. Pressure distribution in the cavity for different positions of the fluid-porous interface, $Re = 100$, Porous media, $\epsilon_{\text{micro}} = 0.9$, $\kappa_{\text{micro}} = 1 \times 10^{-11} \text{ m}^2$).

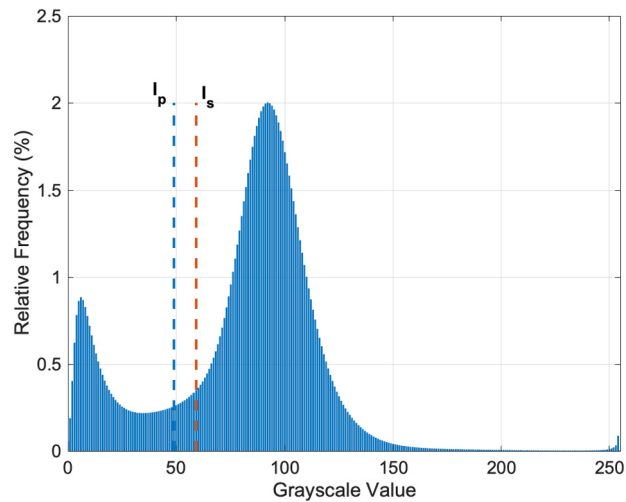


Fig. 20. Distribution of Grayscale Value.

previous considerations about the importance of mesh resolution at interface between regions with different permeability, we estimate that a micro-CT image with a resolution of the order of the micrometer (which is generally the case) is fine enough. Sometimes, according to the case, a mesh refinement by splitting each voxel of the micro-CT images into several cells of the computational grid or a micro-CT images with smaller resolution will be required.

In the proposed method velocity and pressure are defined on the nodes, while the porosity values, derived from micro-CT images, are defined on the cells centre. We assume that the value of the porosity at one node is equal to the average of the porosity values of the cells surrounding it (four cells in 2D and 8 cells in 3D).

Computational settings

To compute the flow, Soulaire et al. [13] proposed to consider the solid rock as a porous media with a very small permeability. It was shown that no-slip boundary conditions can be reproduced at the solid walls if the permeability of the porous region is small enough [14]. This method is computationally expensive. In our work, to make the proposed method valid all over the computational domain, i.e. in the free and the solid regions and to save computational power, the cells describing solid regions are not computed. The boundary conditions at the pore-solid interface are set to be non-slip (zero normal and tangential velocity) boundary conditions [1,2].

A pressure difference, ΔP , is imposed on the inlet and outlet sides of the sample for the simulation. Non-slip boundary conditions are applied on the remaining faces [62]. The transient behaviour depends on the initial condition. We applied initial conditions:

$$\begin{aligned} u(x, t = 0) &= 0 \\ p(x, t = 0) &= \Delta P \frac{x}{L} \end{aligned} \quad (42)$$

with u the velocity, p the pressure, ΔP the pressure gradient magnitude and L the domain size. The fluid is assumed to be water with dynamic viscosity $\mu = 1.0 \times 10^{-3} \text{ Pa.s}$ and the density is $\rho = 1.0 \times 10^3 \text{ kg.m}^{-3}$, the pressure drop is set to be 1.0 Pa .

Calculation of permeability

The effective permeability tensor $\kappa = \kappa_{ij}$ is calculated by using the Darcy equation:

$$\kappa_{ij} = \frac{J_i \mu}{\nabla P_j} \quad i, j = x, y, z \quad (43)$$

where J_i is the flowrate in the i^{th} direction and ∇P_j is the pressure gradient in the j^{th} direction.

J is computed:

$$J_i = \frac{1}{V_\Omega} \int_{\Omega} u_i d\Omega \quad i = x, y, z \quad (44)$$

where Ω is the whole sample considered, V_Ω is the whole volume of the sample and u_i the flow velocity in the i^{th} direction. Usually, permeability κ is expressed in Darcy with $1 \text{ Darcy} = 9.869 \times 10^{-13} \text{ m}^2$.

MPI parallelism

MPI parallelism was used by decomposing the domain in several subdomains according to a 3-dimensional Cartesian grid. The division was done in such way that each subdomain created contains almost the same number of cells to allow a good load balance. Fig. 21 and Fig. 22 illustrate the decomposition of a 3-dimensional domain with a $3 \times 3 \times 3$ grid (27 subdomains).

Influence of micro-porosity

To investigate the influence of micro porosity on pore-scale flow simulations, a sub sample of size 150^3 was extracted from the entire sample and segmented into three different phases: void, solid, and micro porous. In this subdomain, the fractions of the different phases are: 81.8%, 15.6%, and 2.4% for the solid, macro-porous, and micro-porous phases respectively.

Fig. 23 shows the maps of micro-porous regions of the considered segmentation. It can be seen that the micro-porous regions are located around the pore spaces. The micro-porous regions allow to increase the size of the pore-throats or allow to connect pore spaces that were initially isolated. The micro-porous region is assumed to have the same micro-porosity ϵ_{micro} . The micro-permeability κ_{micro} associated is estimated using the Kozeny-Carman relation (41).

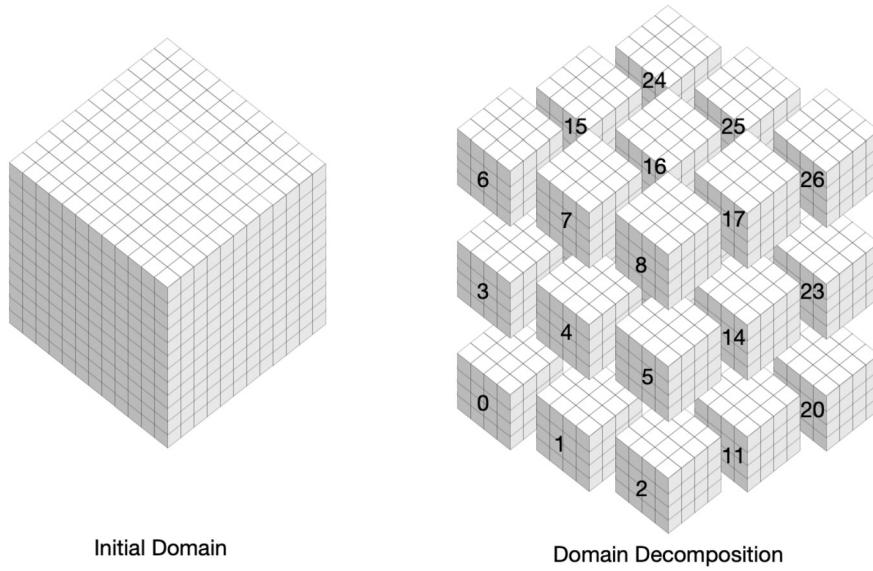


Fig. 21. Schematic description of a 3-dimensional domain decomposition using 27 subdomains ($3 \times 3 \times 3$ Grid), numbered from 0–26.

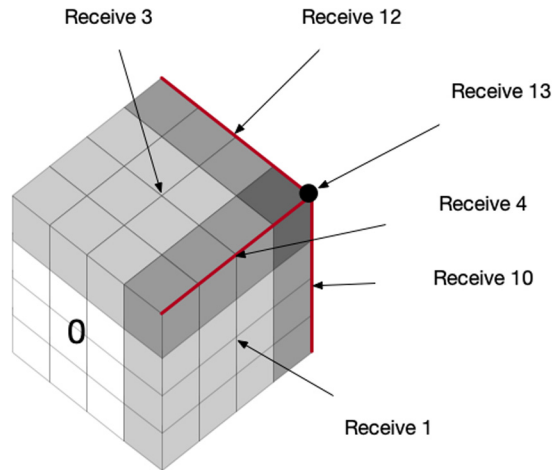


Fig. 22. Schematic representation of the MPI communications for the process of rank 0 in a $3 \times 3 \times 3$ grid (27 subdomains).

Table 1

Summary of simulation results for different micro-porosity values.

ϵ_{micro}	0	0.25	0.5	0.75	0.9	1
κ_{micro} (mD)	0	0.79	14.2	192	2080	∞
κ_{xx}	289	338	373	405	435	462

Several simulations are performed for ϵ_{micro} ranging from 0 to 1. For these two extremes, the computed permeability is 289 and 462 mD, respectively. These two limit values of ϵ_{micro} denote specific situations, whereby the micro-porous phase is identified as fully solid ($\epsilon_{\text{micro}} = 0$) or fully void ($\epsilon_{\text{micro}} = 1$). Table 1 presents the computed permeability, κ_{xx} for different values of the micro-porosity ϵ_{micro} . As expected, κ_{xx} increases when the micro-porosity increases in the micro-porous region. The results clearly show that the computed absolute value depends a lot on the segmentation. Different segmentation can lead to computed permeability up to 50% larger or smaller. For this subsample, the permeability value obtained when the micro-porosity is distributed and proportional to the gray level lies between the bounding values and was estimated to be 394 mD. It can be seen that even for a micro-porous region that represents 2.4% of the total volume, its influence on the computed permeability is not negligible. Fig. 24 shows the convergence history and time steps required. Compared with standard implicit solver, it requires more iterations steps but less memory. From the practical point of view, these approaches will be attractive for the image simulation $500^3 - 1000^3$, which can be handled in a workstation.

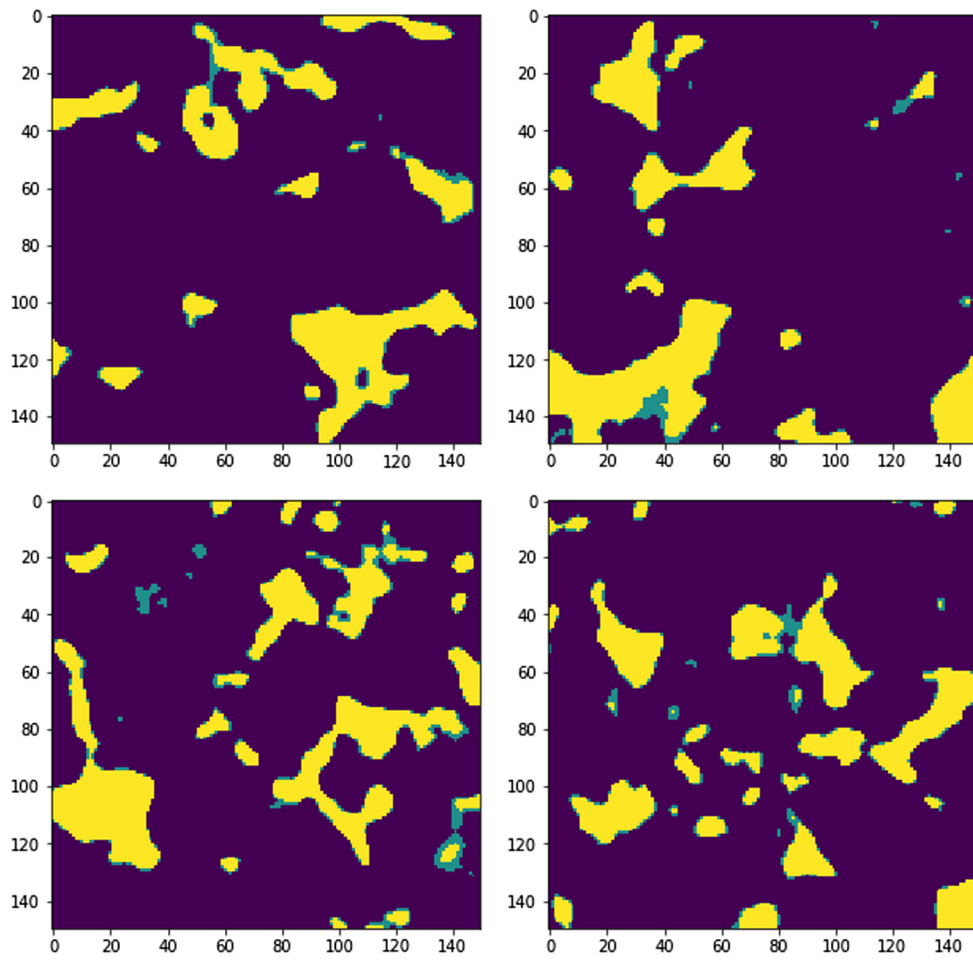


Fig. 23. Map of the micro-porous regions for subsample (black = solid, yellow = void, green = micro-porosity).

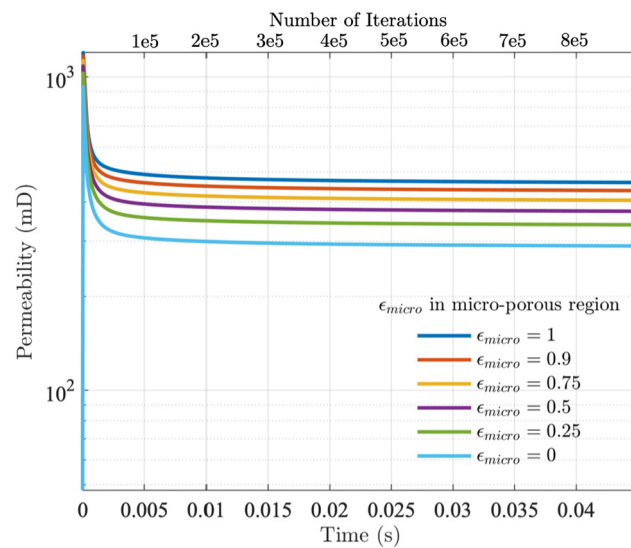


Fig. 24. Computed Permeability with homogeneous micro-porous region.

Table 2
Properties of the subsamples considered.

	Size	Solid (%)	Macro-porosity (%)	Micro-porosity (%)
Subsample 1	500 ³	79.2	18.4	2.4
Subsample 2	500 ³	79.5	18.0	2.5

Table 3
Effective Permeability K_{xx} (mD) computed.

	$\epsilon_{\text{micro}} = 0$	$\epsilon_{\text{micro}} = 1$	ϵ_{micro} based on Grayscale
Subsample 1	400	597	519
Subsample 2	369	564	485

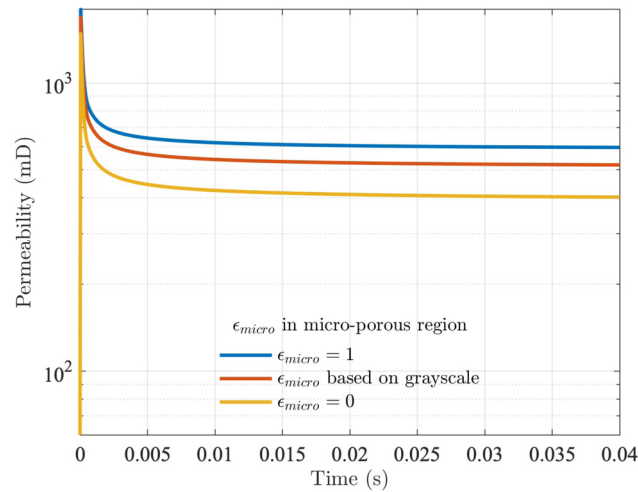


Fig. 25. Computed Permeability.

Results with the use of a distributed micro-porosity field

The situation presented above allows to emphasise well the influence of micro-porous region on the computed permeability. But considering the same micro-porosity ϵ_{micro} in the entire rock sample is not realistic. In general, the micro-porosity field takes values that are heterogeneously distributed in the rock. In this section, the micro-porosity field, ϵ_{micro} , is defined with the gray level of the micro-CT images using the relation (40). The micro-permeability κ_{micro} associated is estimated using the Kozeny-Carman relation (41) (Table 3). We have extracted different subsamples of size 500³ whose properties are summarised in Table 2.

These simulations show that although this Berea Sandstone contains only 2% of micro-porosity, its influence on computed permeability is already significant. A higher impact is expected for complex multi-scale rocks such as carbonates that are likely to present a high ratio of micro-porosity (up to 10%), shown in Fig. 25.

Fig. 26 displays the micro-porosity distribution, the velocity-magnitude distribution and the pressure field in the void space taken in the flow direction. Fig. 26a shows that micro-porous region (in blue) allows to widen or linked macro-porous region (in red) allowing the development of the velocity and pressure field in these regions.

Influence of the subsample considered

In this section we compare the influence of the domain size considered. For this we consider two concentric subsamples of size 500³ and 800³ respectively (see Fig. 27 and Table 4).

For the sub-sample 3, the effective permeability computed based on grayscale is 559 mD, while for the sub-sample 2, the effective permeability computed based on grayscale is 485 mD. The results show clearly that the sample considered is not homogeneous. It shows the difficulty to determine a right representative element of volume (REV) of the whole rock field. However, all simulations done were consistent with computed permeability varying around 400–500 mD.

In this work, the computational grid was directly derived from the micro-CT images (voxel grid and computational grid are the same) and we assumed that the resolution of the micro-CT images used was fine enough to provide accurate results. However, it is known that the permeability computations of micro-CT images are very sensitive to the image and

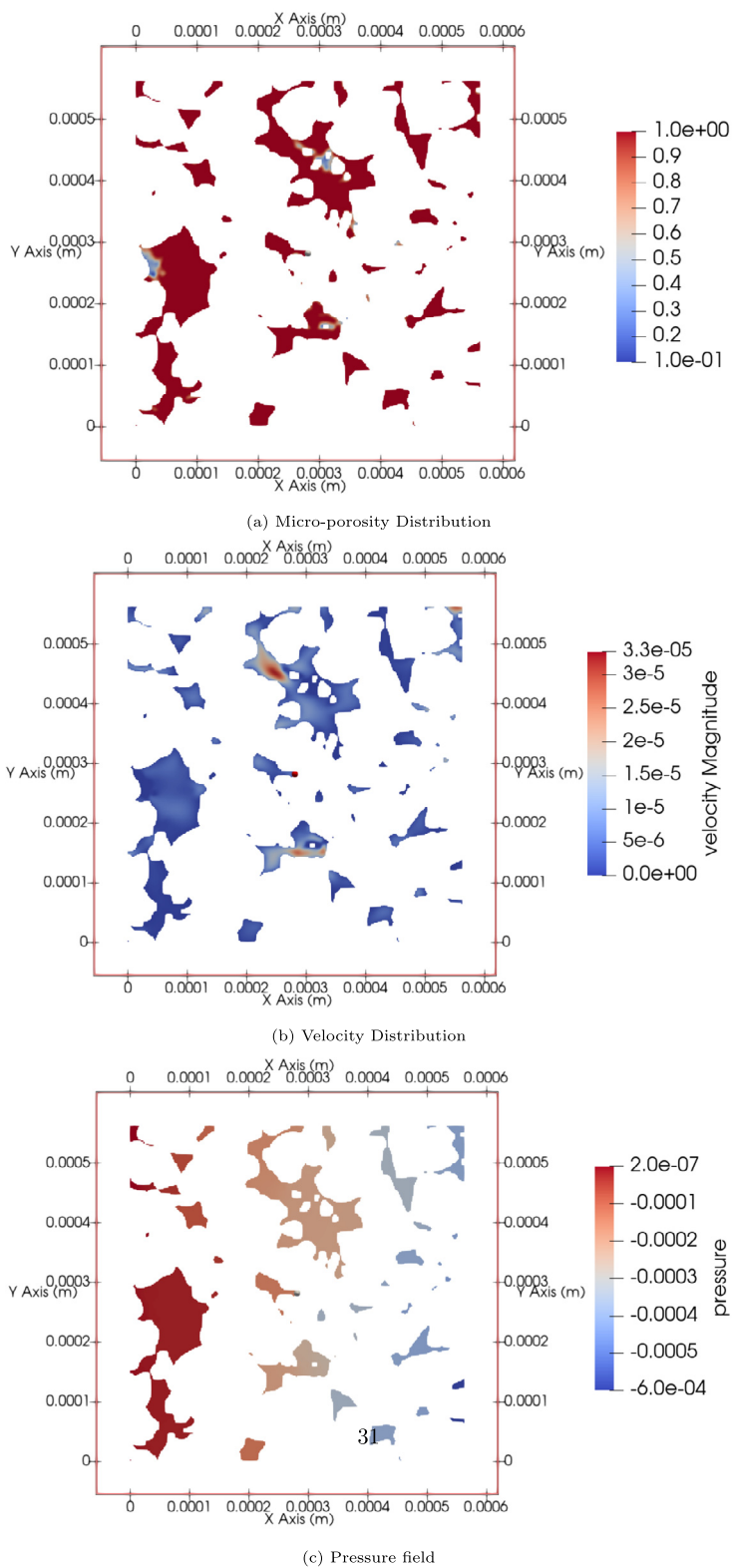


Fig. 26. Plot of the simulation results for Subsample 1 (500³), slice 250 × 250 in the flow direction.

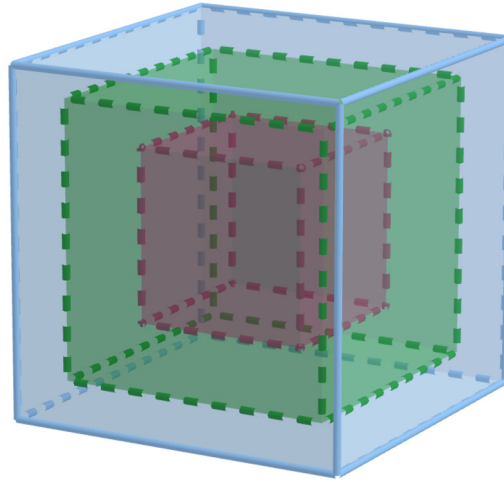


Fig. 27. Whole domain (1000^3) in blue and the 2 subsamples considered: subsample 2 (500^3) in red and subsample 3 (800^3) in green.

Table 4
Properties of the subsamples considered.

	Size	Solid (%)	Macro-porosity (%)	Micro-porosity (%)
Subsample 2	500^3	79.5	18.0	2.5
Subsample 3	800^3	78.4	19.0	2.6

mesh resolutions. Indeed, as noted by [19] the cell size has to be of the order of $\sqrt{\kappa_{\text{micro}}}$ to resolve the transition zone at the interface, where the flow changes drastically. Further work has thus to be done to assess the permeability accuracy dependence with the mesh resolution. For example, [63] investigated on the effects of image resolution and numerical resolution on computed permeability using FEM pore-scale simulations. They show how changes in computed permeability are affected by image resolution (which dictates how well the pore geometry is approximated) versus grid or mesh resolution (which changes numerical accuracy). Their results show that performing grid coarsening on the FEM mesh caused a reduction in computed permeability. However, they noted that in their case this effect was related to tightening of the pore space rather than loss of numerical accuracy. They concluded that a due attention must be paid to the quality of the images that are provided for running pore-scale simulations. The quality of these images is one of the most important factors affecting the quality of the simulation results. It might be a good practice to generate images with different resolutions and check the influence of image resolutions on the results. For a given image, it would be great to carry out the simulations using different computational grids and check the dependence of the results on it.

Only one a Berea sandstone sample is assessed. This kind of rock is known to contain a low fraction of sub-voxel porosity, but its influence on permeability computation is already significant [2]. A higher impact is expected for complex multi-scale rocks such as carbonates that are likely to present a higher ratio of micro-porosity, and hence that may display a significant fraction of sub-voxel porosity, even when the samples are scanned with high resolution [64,65].

6. Conclusions

We proposed a new method to solve the Navier-Stokes-Brinkman system on grayscale micro-CT images. The method was based on a fully explicit stabilised finite element solver for the Navier-Stokes-Brinkman flow in which the Darcy term was treated implicitly to avoid time stepping stability restriction. This novel algorithm shows excellent efficiency and numerical stability especially near the interface of fluid-porous region where large velocity/pressure gradient can be observed. The proposed model has been benchmarked by several well-known 2-dimensional cases and the influence of the stabilisation parameter and the grid size have been studied.

We solved the 3-dimensional grayscale micro-CT images up to 800^3 using hybrid OpenMP/MPI implementation. The explicit node-based algorithm is ideal for image-based calculation. The memory cost of this algorithm is low due to the trilinear continuous velocity space and matrix-free implementation. We used the model to estimate absolute permeability on micro-CT images of a Berea Sandstone. The influence of micro-porosity has been studied on the effective permeability computed. It has been shown that even a small fraction of micro-porous regions has a significant impact on the effective permeability computed.

CRediT authorship contribution statement

Loic Balazi Atchy Nillama: Formal analysis, Investigation, Software, Visualization, Writing – original draft. **Jianhui Yang:** Conceptualization, Methodology, Project administration, Resources, Software, Supervision, Writing – review & editing. **Liang Yang:** Conceptualization, Methodology, Project administration, Resources, Software, Supervision, Writing – review & editing.

Declaration of competing interest

The authors declare that they have no known competing financial interests or personal relationships that could have appeared to influence the work reported in this paper.

Acknowledgements

We are grateful to the EPSRC ARCHER2 instant access grant Q1396010. The authors would like to thank TOTAL management for the authorisation to publish this work.

References

- [1] M.J. Blunt, *Multiphase Flow in Permeable Media: A Pore-Scale Perspective*, Cambridge University Press, Cambridge, 2019.
- [2] C. Soulaire, F. Gjetvåg, C. Garing, S. Roman, A. Russian, P. Gouze, H.A. Tchelepi, The impact of sub-resolution porosity of X-ray microtomography images on the permeability, *Transp. Porous Media* 113 (1) (2016) 227–243.
- [3] X. Meng, L. Wang, W. Zhao, X. Yang, Simulating flow in porous media using the lattice Boltzmann method: intercomparison of single-node boundary schemes from benchmarking to application, *Adv. Water Resour.* 141 (2020), <https://doi.org/10.1016/j.advwatres.2020.103583>.
- [4] T. Akai, M. Blunt, B. Bijeljic, Pore-scale numerical simulation of low salinity water flooding using the lattice Boltzmann method, *J. Colloid Interface Sci.* 566 (2020) 444–453, <https://doi.org/10.1016/j.jcis.2020.01.065>.
- [5] T. Ramstad, A. Kristoffersen, E. Ebeltoft, Uncertainty span for relative permeability and capillary pressure by varying wettability and spatial flow directions utilizing pore scale modelling, vol. 146, <https://doi.org/10.1051/e3sconf/202014601002>, 2020.
- [6] R. Song, Y. Wang, J. Liu, M. Cui, Y. Lei, Comparative analysis on pore-scale permeability prediction on micro-CT images of rock using numerical and empirical approaches, *Energy Sci. Eng.* 7 (6) (2019) 2842–2854, <https://doi.org/10.1002/ese3.465>.
- [7] F. Alpak, F. Gray, N. Saxena, J. Dietrich, R. Hofmann, S. Berg, A distributed parallel multiple-relaxation-time lattice Boltzmann method on general-purpose graphics processing units for the rapid and scalable computation of absolute permeability from high-resolution 3D micro-CT images, *Comput. Geosci.* 22 (3) (2018) 815–832, <https://doi.org/10.1007/s10596-018-9727-7>.
- [8] M. Zambrano, E. Tondi, L. Mancini, G. Lanzafame, F. Trias, F. Arzilli, M. Materazzi, S. Torrieri, Fluid flow simulation and permeability computation in deformed porous carbonate grainstones, *Adv. Water Resour.* 115 (2018) 95–111, <https://doi.org/10.1016/j.advwatres.2018.02.016>.
- [9] J. Zhu, J. Ma, An improved gray lattice Boltzmann model for simulating fluid flow in multi-scale porous media, *Adv. Water Resour.* 56 (2013) 61–76.
- [10] M. Starnoni, D. Pokrajac, J. Neilson, Computation of fluid flow and pore-space properties estimation on micro-CT images of rock samples, *Comput. Geosci.* 106 (2017) 118–129, <https://doi.org/10.1016/j.cageo.2017.06.009>.
- [11] M. Tembely, A. Alsumaiti, K. Rahimov, M. Jouini, Numerical simulation of non-Newtonian fluid flow through a rock scanned with high resolution X-ray micro-CT 2230 (2017) 958–960.
- [12] M. Liu, P. Mostaghimi, High-resolution pore-scale simulation of dissolution in porous media, *Chem. Eng. Sci.* 161 (2017) 360–369, <https://doi.org/10.1016/j.ces.2016.12.064>.
- [13] C. Soulaire, S. Roman, A. Kovscek, H.A. Tchelepi, Mineral dissolution and wormholing from a pore-scale perspective, *J. Fluid Mech.* 827 (2017) 457–483.
- [14] C. Soulaire, H.A. Tchelepi, Micro-continuum approach for pore-scale simulation of subsurface processes, *Transp. Porous Media* 113 (3) (2016) 431–456, <https://doi.org/10.1007/s11242-016-0701-3>.
- [15] L. Yang, J. Yang, E. Boek, M. Sakai, C. Pain, Image-based simulations of absolute permeability with massively parallel pseudo-compressible stabilised finite element solver, *Comput. Geosci.* (2019) 1–13.
- [16] M. Krotkiewski, I. Ligaarden, K.-A. Lie, D.W. Schmid, On the importance of the Stokes-Brinkman equations for computing effective permeability in karst reservoirs, *Commun. Comput. Phys.* 10 (5) (2011) 1315–1332.
- [17] T. Karper, K.-A. Mardal, R. Winther, Unified finite element discretizations of coupled Darcy–Stokes flow, *Numer. Methods Partial Differ. Equ.* 25 (2) (2009) 311–326, <https://doi.org/10.1002/num.20349>.
- [18] A. Gulbransen, V. Hauge, K.-A. Lie, A multiscale mixed finite-element method for vuggy and naturally fractured reservoirs, *SPE J.* 15 (10) (2008).
- [19] F. Kazunori, M. Akira, Numerical analysis of coupled flows in porous and fluid domains by the Darcy-Brinkman equations, *Soil Found.* 58 (5) (2018) 240–259.
- [20] M. Ehrhardt, An introduction to fluid-porous interface coupling, in: *Progress in Computational Physics*, vol. 2, 2012.
- [21] S. Badia, R. Codina, Unified stabilized finite element formulations for the Stokes and the Darcy problems, *SIAM J. Numer. Anal.* 47 (3) (2009) 1971–2000.
- [22] A. Masud, T.J. Hughes, A stabilized mixed finite element method for Darcy flow, *Comput. Methods Appl. Mech. Eng.* 191 (39–40) (2002) 4341–4370.
- [23] A. Masud, A stabilized mixed finite element method for Darcy–Stokes flow, *Int. J. Numer. Methods Fluids* 54 (6–8) (2007) 665–681.
- [24] S. Badia, R. Codina, Stabilized continuous and discontinuous Galerkin techniques for Darcy flow, *Comput. Methods Appl. Mech. Eng.* 199 (2008) 1654–1667.
- [25] G. Buscaglia, F. Basombrío, R. Codina, Fourier analysis of an equal-order incompressible flow solver stabilized by pressure gradient projection, *Int. J. Numer. Methods Fluids* 34 (1) (2000) 65–92, [https://doi.org/10.1002/1097-0363\(20000915\)34:1<65::AID-FLD56>3.0.CO;2-J](https://doi.org/10.1002/1097-0363(20000915)34:1<65::AID-FLD56>3.0.CO;2-J).
- [26] D. Schötzau, C. Schwab, Exponential convergence in a Galerkin least squares hp-FEM for Stokes flow, *IMA J. Numer. Anal.* 21 (1) (2001) 53–80, <https://doi.org/10.1093/imanum/21.1.53>.
- [27] Y.-T. Wei, J.-H. Yu, P. Geubelle, A comparative study of different GLS elements for solving incompressible viscous flows 41 (2009) 60–67.
- [28] C. Huang, Y. Bao, D. Zhou, J.-Q. Xu, Large Eddy simulation for wind field analysis based on stabilized finite element method, *J. Zhejiang Univ. Sci. A* 12 (4) (2011) 278–290, <https://doi.org/10.1631/jzus.A1000114>.
- [29] M. Olshanskii, A. Reusken, X. Xu, A stabilized finite element method for advection-diffusion equations on surfaces, *IMA J. Numer. Anal.* 34 (2) (2014) 732–758, <https://doi.org/10.1093/imanum/drt016>.
- [30] S. Aydin, M. Tezer-Sezgin, Stabilizing subgrid FEM solution of the natural convection flow under high magnitude magnetic field on sinusoidal corrugated enclosure, *Int. J. Comput. Math.* 97 (1–2) (2020) 420–430, <https://doi.org/10.1080/00207160.2019.1636232>.

- [31] S. Nagaoka, Y. Nakabayashi, G. Yagawa, Fluid-structure coupled analysis using enriched free mesh method, *Key Eng. Mater.* 462–463 (2011) 1238–1243, <https://doi.org/10.4028/www.scientific.net/KEM.462-463.1238>.
- [32] S. Nagaoka, Y. Nakabayashi, G. Yagawa, Parallelization of enriched free mesh method for large scale fluid-structure coupled analysis, *Proc. Eng.* 90 (2014) 288–293, <https://doi.org/10.1016/j.proeng.2014.11.851>.
- [33] E. Gawronska, R. Dyja, 3D simulations of solidification with liquid phase flow, *IOP Conf. Ser., Mater. Sci. Eng.* 776 (1) (2020), <https://doi.org/10.1088/1757-899X/776/1/012029>.
- [34] T. He, Stabilization of a smoothed finite element semi-implicit coupling scheme for viscoelastic fluid–structure interaction, *J. Non-Newton. Fluid Mech.* 292 (2021), <https://doi.org/10.1016/j.jnnfm.2021.104545>.
- [35] T. He, The cell-based smoothed finite element method for viscoelastic fluid flows using fractional-step schemes, *Comput. Struct.* 222 (2019) 133–147, <https://doi.org/10.1016/j.compstruc.2019.07.007>.
- [36] R. Codina, Stabilized finite element approximation of transient incompressible flows using orthogonal subscales, *Comput. Methods Appl. Mech. Eng.* 191 (2002) 4295–4321.
- [37] R. Codina, J. Blasco, Analysis of a stabilized finite element approximation of the transient convection-diffusion-reaction equation using orthogonal subscales, *Comput. Vis. Sci.* 4 (3) (2002) 167–174, <https://doi.org/10.1007/s007910100068>.
- [38] S. Badia, R. Codina, On a multiscale approach to the transient Stokes problem: dynamic subscales and anisotropic spacetime discretization, *Appl. Math. Comput.* 2007 (2) (2009) 415–433.
- [39] T.J. Hughes, G.R. Feijóo, L. Mazzei, J.-B. Quincy, The variational multiscale method—a paradigm for computational mechanics, in: *Advances in Stabilized Methods in Computational Mechanics*, *Comput. Methods Appl. Mech. Eng.* 166 (1) (1998) 3–24, [https://doi.org/10.1016/S0045-7825\(98\)00079-6](https://doi.org/10.1016/S0045-7825(98)00079-6).
- [40] T. Tezduyar, *Stabilized Finite Element Formulations for Incompressible Flow Computations*, in: J.W. Hutchinson, T.Y. Wu (Eds.), *Advances in Applied Mechanics*, vol. 28, Elsevier, 1991.
- [41] F. Brezzi, M.-O. Bristeau, L.P. Franca, M. Mallet, G. Rogé, A relationship between stabilized finite element methods and the Galerkin method with bubble functions, *Comput. Methods Appl. Mech. Eng.* 96 (1) (1992) 117–129, [https://doi.org/10.1016/0045-7825\(92\)90102-P](https://doi.org/10.1016/0045-7825(92)90102-P), <https://www.sciencedirect.com/science/article/pii/004578259290102P>.
- [42] L.P. Franca, S.L. Frey, T.J.R. Hughes, Stabilized finite element methods: I. Application to the advective-diffusive model, *Comput. Methods Appl. Mech. Eng.* 95 (2) (1992) 253–276, [https://doi.org/10.1016/0045-7825\(92\)90143-8](https://doi.org/10.1016/0045-7825(92)90143-8), <https://www.sciencedirect.com/science/article/pii/0045782592901438>.
- [43] T.J.R. Hughes, Multiscale phenomena: Green's functions, the Dirichlet-to-Neumann formulation, subgrid scale models, bubbles and the origins of stabilized methods, *Comput. Methods Appl. Mech. Eng.* 127 (1–4) (1995) 387–401.
- [44] L. Yang, S. Badia, R. Codina, A pseudo-compressible variational multiscale solver for turbulent incompressible flows, *Comput. Mech.* 58 (6) (2016) 1051–1069.
- [45] R.d. Borst, E. Ramm, *Multiscale Methods in Computational Mechanics: Progress and Accomplishments*, Springer Science & Business Media, 2010, Google-Books-ID: BDZ5PwUwhKwC.
- [46] A. Domaingo, D. Langmayr, B. Somogyi, R. Almbauer, A semi-implicit treatment of porous media in steady-state cfd, *Transp. Porous Media* 112 (2) (2016) 451–466, <https://doi.org/10.1007/s11242-016-0657-3>.
- [47] M. Komijani, R. Gracie, An enriched finite element model for wave propagation in fractured media, *Finite Elem. Anal. Des.* 125 (2017) 14–23, <https://doi.org/10.1016/j.finel.2016.11.001>, <https://www.sciencedirect.com/science/article/pii/S0168874X16305248>.
- [48] M. Ainsworth, Dispersive behaviour of high order finite element schemes for the one-way wave equation, *J. Comput. Phys.* 259 (2014) 1–10, <https://doi.org/10.1016/j.jcp.2013.11.003>, <https://www.sciencedirect.com/science/article/pii/S0021999113007493>.
- [49] R. Shamasundar, W.A. Mulder, Improving the accuracy of mass-lumped finite-elements in the first-order formulation of the wave equation by defect correction, *J. Comput. Phys.* 322 (2016) 689–707, <https://doi.org/10.1016/j.jcp.2016.07.006>, <https://www.sciencedirect.com/science/article/pii/S0021999116302856>.
- [50] J.-L. Guermond, R. Pasquetti, A correction technique for the dispersive effects of mass lumping for transport problems, *Comput. Methods Appl. Mech. Eng.* 253 (2013) 186–198, <https://doi.org/10.1016/j.cma.2012.08.011>, <https://linkinghub.elsevier.com/retrieve/pii/S0045782512002630>.
- [51] A. Pal, A. Agarwala, S. Raha, B. Bhattacharya, Performance metrics in a hybrid MPI–OpenMP based molecular dynamics simulation with short-range interactions, *J. Parallel Distrib. Comput.* 74 (3) (2014) 2203–2214, <https://doi.org/10.1016/j.jpdc.2013.12.008>, <https://www.sciencedirect.com/science/article/pii/S07437371513002505>.
- [52] R. Brown, I. Sharapov, High-scalability parallelization of a molecular modeling application: performance and productivity comparison between OpenMP and MPI implementations, *Int. J. Parallel Program.* (2007), <https://doi.org/10.1007/s10766-007-0057-y>.
- [53] G. Krawezik, F. Cappello, Performance comparison of MPI and OpenMP on shared memory multiprocessors, *Concurr. Comput., Pract. Exp.* 18 (2006) 29–61, <https://doi.org/10.1002/cpe.905>.
- [54] U. Ghia, K.N. Ghia, C. Shin, High-re solutions for incompressible flow using the Navier-Stokes equations and a multigrid method, *J. Comput. Phys.* 48 (3) (1982) 387–411.
- [55] U. Ghia, K. Ghia, C. Shin, High-re solutions for incompressible flow using the Navier-Stokes equations and a multigrid method, *J. Comput. Phys.* 48 (3) (1982) 387–411, [https://doi.org/10.1016/0021-9991\(82\)90058-4](https://doi.org/10.1016/0021-9991(82)90058-4).
- [56] R. Neumann, M. Andreetta, E. Lucas-Oliveira, 11 sandstones: raw, filtered and segmented data, <http://www.digitalrockportal.org/projects/317>, 2020, <https://doi.org/10.17612/f4h1-w124>.
- [57] R.F. Neumann, M. Barsi-Andreetta, E. Lucas-Oliveira, H. Barbalho, W.A. Trevizan, T.J. Bonagamba, M. Steiner, High accuracy capillary network representation in digital rock reveals permeability scaling functions, *arXiv:2010.10679*, 2020.
- [58] D.H. Kang, E. Yang, T.S. Yun, Stokes-Brinkman flow simulation based on 3-D μ -ct images of porous rock using grayscale pore voxel permeability, *Water Resour. Res.* 55 (5) (2019) 4448–4464.
- [59] Q. Lin, Y. Al-Khulaifi, M.J. Blunt, B. Bijeljic, Quantification of sub-resolution porosity in carbonate rocks by applying high-salinity contrast brine using X-ray microtomography differential imaging, *Adv. Water Resour.* 96 (2016) 306–322.
- [60] R. Sok, T. Varslot, A. Ghous, S. Latham, A. Sheppard, M. Knackstedt, Pore scale characterization of carbonates at multiple scales: integration of micro-ct, bsem, and fibsem, *Petrophysics* 51 (12 2010).
- [61] C. Noiriell, D. Bernard, P. Gouze, X. Thibault, Hydraulic properties and microgeometry evolution accompanying limestone dissolution by acidic water, *Oil Gas Sci. Technol.* 60 (2005) 177–192, <https://doi.org/10.2516/ogst:2005011>.
- [62] R. Guibert, P. Horgue, G. Debenest, M. Quintard, A comparison of various methods for the numerical evaluation of porous media permeability tensors from pore-scale geometry, *Math. Geosci.* 48 (3) (2016) 329–347, <https://doi.org/10.1007/s11004-015-9587-9>.
- [63] A.T. Borujeni, N.M. Lane, K. Thompson, M. Tyagi, Effects of image resolution and numerical resolution on computed permeability of consolidated packing using LB and FEM pore-scale simulations, *Comput. Fluids* 88 (2013) 753–763, <https://doi.org/10.1016/j.compfluid.2013.05.019>, <https://www.sciencedirect.com/science/article/pii/S0045793013002119>.

- [64] C. Garing, L. Luquot, P. Pezard, P. Gouze, Electrical and flow properties of highly heterogeneous carbonate rocks, AAPG Bull. (Jun. 2013), <https://doi.org/10.1306/05221312134>.
- [65] V. Hebert, C. Garing, L. Luquot, P. Pezard, P. Gouze, Multi-scale X-ray tomography analysis of carbonate porosity, in: Fundamental Controls on Fluid Flow in Carbonates: Current Workflows to Emerging Technologies, in: Geological Society Special Publication, vol. 406, 2015, pp. 61–79, <https://hal.archives-ouvertes.fr/hal-01174157>.